SEDIMENTOLOGY the journal of the International Association of Sedimentologists

Sedimentology (2021) **68**, 2097–2124 doi: 10.1111/sed.12845

Evolution of foreland basin fluvial systems in the mid-Cretaceous of Utah, USA (upper Cedar Mountain and Naturita formations)

STEPHEN P. PHILLIPS*, JOHN A. HOWELL†, ADRIAN J. HARTLEY†, MAGDA CHMIELEWSKA† and SAMUEL M. HUDSON*

**Department of Geological Sciences, S389 Eyring Science Center, Provo, UT, 84602, USA*

†Department of Geology and Petroleum Geology, University of Aberdeen, Meston Building, Aberdeen, AB24 3UE, UK (E-mail: sphill25@byu.edu)

Associate Editor – Christopher Fielding

ABSTRACT

An analysis of the sedimentary fill of a foreland basin can provide information on the relative effect of tectonics, base-level fluctuations and climate during basin development. This study analyzes fluvial strata from the upper Cedar Mountain and Naturita formations of the mid-Cretaceous foreland basin of Utah (USA) to determine the effects of spatial location within the foreland basin on fluvial planform and architecture. The study results document consistent planform and architecture across the distal foredeep and forebulge depozones during flooding of the Western Interior Seaway suggesting that fluvial planform and architecture did not change as a function of position within foreland basin depozone or as a result of base-level rise. Outcrop data, virtual outcrop models and satellite imagery were used to perform facies and architectural analysis and to collect dimensional and geometric data. Fluvial channel deposits consist of coarse-grained, laterally accreting bars deposited within narrow, low to moderate sinuosity channels, that were vertically stacked and encased in floodplain fines regardless of geographic location or stratigraphic position and may represent distal deposits of a distributive fluvial system. Bar elements increased in thickness over time indicating increasing channel depths and enhanced discharge. Palaeohydraulic calculations indicate an increase in discharge from between 315 and 1023 to between 1896 and 5270 m^3/s, likely due to enhanced precipitation and/or drainage capture in the catchment and basin. Calculated drainage areas for the system increased from 10^4 to 10^5 km^2 scale over time. The uppermost fluvial deposits were in close proximity (≤60 km) to contemporaneous shoreface systems as the Western Interior Seaway expanded; yet backwater effects are not observed, suggesting that rising base level had no significant effect on fluvial planform or architecture. These results show that fluvial planform and architecture remained constant despite rising base-level, changing climate, increased discharge and position in different foreland basin depozones.

Keywords Architectural analysis, distributive fluvial system, facies analysis, foreland basin, palaeohydraulics.

INTRODUCTION

An understanding of sedimentary architecture and stacking patterns in subsiding and evolving basins is important for many reasons. An analysis of trends in these variables can aid current understanding of the dominant controls on sedimentation, such as: subsidence rates and accommodation, sediment supply, climate change or base level-changes (e.g. Mackin, 1948; Leopold & Bull, 1979; Posamentier & Vail, 1988; Shanley & McCabe, 1991; Currie, 1997, 1998). Additionally, it aids in the ability to be predictive relative to the size, geometry and occurrence of subsurface reservoirs.

The aim of this study is to evaluate the effect of foreland basin tectonics, base-level rise and climate change on fluvial architecture during basin-scale flooding. The specific objectives for the study are to document any changes in fluvial planform or architecture down-dip and through time, track changes in climate by facies analysis and palaeohydraulic estimations, evaluate the effect of base-level rise on nearshore channel architecture, and build a depositional model for the system.

The upper Cedar Mountain and Naturita formations (Dakota Sandstone) are an excellent example of a low net to gross (10 to 20%) fluvial and estuarine system deposited in a developing foreland basin across the foredeep to forebulge transition (DeCelles & Currie, 1996; Currie, 1997). New dimensional and geometric data allow analysis of the relative effects of subsidence, eustacy and climate on aggradational fluvial systems. The study interval records significant changes in channel size, palaeodischarge and palaeodrainage of fluvial systems yet exhibits no change in fluvial planform or architecture. This study aims to provide a facies and architectural analysis that spans the foredeep to forebulge transition (*ca* 180 km across). As such, it is focused on basin-scale variations in fluvial style, architecture and palaeohydraulics derived from new, quantitative dimensional data. The study builds upon work that previously delineated foreland basin depozones, described the geometry of the clastic wedge, and developed nonmarine to marine sequence stratigraphic concepts (Currie, 1997).

The Cedar Mountain and Naturita formation interval has achieved significant interest for its exceptionally well-preserved and exposed channel belts that can be viewed in three dimensions (e.g. Harris, 1980; Nuse, 2015; Speed *et al.*, 2019; Cardenas *et al.*, 2020) and has been used as an analogue to similar structures on Mars (e.g. Williams *et al.*, 2011; Hayden *et al.*, 2019). The formations have also been the focus of extensive palaeontological research (see Kirkland *et al.*, 2016 for a detailed history). Additionally, the Cedar Mountain Formation has been a significant historical target for oil and gas exploration and production in the Uinta Basin (e.g. Williams, 1961; Vaughn & Picard, 1976; Currie *et al.*, 2008, 2012).

Study area

Within east-central Utah, USA, the Cedar Mountain and Naturita formations are exposed around an anticlinal structure called the San Rafael Swell, along the southern edge of the Uinta Basin and around the northern tip of the Henry Mountains Basin (Fig. 1). Continuous outcrop extends from the south-western portion of the San Rafael Swell, around the northern tip of the San Rafael Swell and eastward from Green River, Utah, to the Colorado River (more than 300 km). This outcrop belt provides an uninterrupted view of foreland basin deposits that span the distal foredeep through the forebulge depozone of the mid-Cretaceous foreland basin system of Utah (Currie, 1997; Fig. 1).

Lithostratigraphy and tectonic setting

The Cedar Mountain Formation is composed of five formal lithostratigraphic members and one informal unit. On the western flank of the San Rafael Swell, listed in ascending order, these members are the Buckhorn Conglomerate, Ruby Ranch Member, informal Short Canyon Conglomerate and Mussentuchit Member (Stokes, 1944; Kirkland *et al.*, 1997, 1999; Doelling & Kuehne, 2013). For the eastern part of the study area, the lithostratigraphic units are, listed in ascending order, the Yellow Cat Member, Poison Strip Member and Ruby Ranch Member (Kirkland *et al.*, 1997, 1999, 2016; Fig. 2). The Cedar Mountain Formation is overlain by the Naturita Formation and unconformably overlies the Brushy Basin Member of the Upper Jurassic Morrison Formation.

The upper members of the Cedar Mountain Formation (Ruby Ranch and Mussentuchit) and the Naturita Formation were deposited in a developing foreland basin. These deposits thicken westward into a foredeep depozone and thin eastward onto a forebulge (Figs 1 and 3;

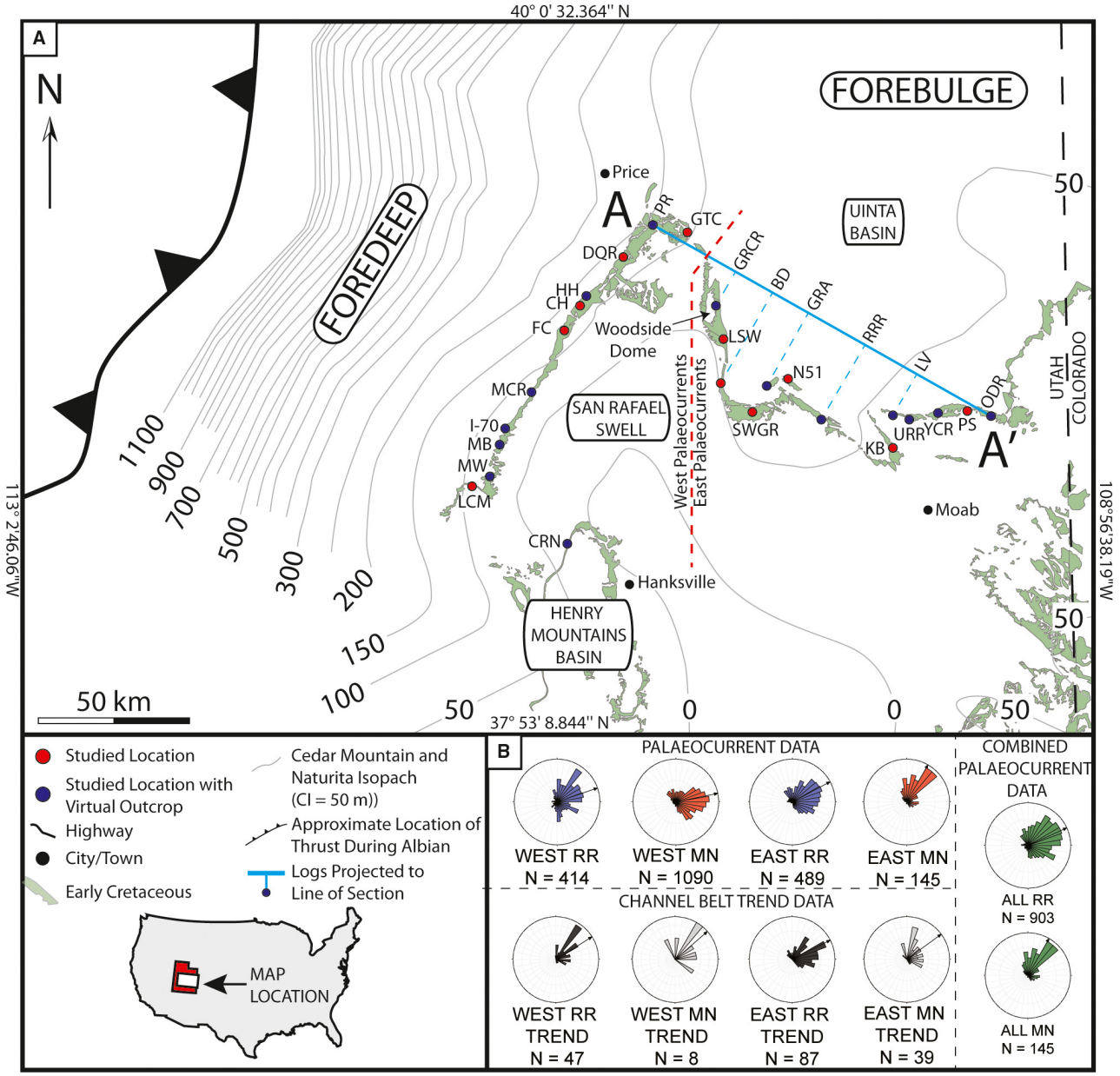

Fig. 1. (A) Early Cretaceous isopach map of eastern Utah showing the foreland basin geometry present in the upper Cedar Mountain and Naturita formations. Notice the westward thickening into the foredeep depozone and eastward thinning onto the forebulge depozone. Isopach values are in metres and are modified from Currie (2002) to include the Naturita Formation. Studied locations are also shown superimposed on the mapped outcrop of the study interval. Line of section A–A′ refers to Fig. 3. (B) Palaeocurrent and channel trend data are reported indicating a north-eastern palaeocurrent direction for the entire interval regardless of geographic region but with local variability. CRN = Caineville Reef North; LCM = Last Chance Monocline; MW = Mussentuchit Wash; MB = Mesa Butte; I-70 = Interstate 70; MCR = Moore Cutoff Road; FC = Ferron Creek; CH = channel; HH = Hadden Holes; DQR = Dinosaur Quarry Road; PR = Price River; GTC = Grassy Trail Creek; GRCR = Green River Cutoff Road; LSW = Lost Spring Wash; BD = Buckmaster Draw; SWGR = South-west Green River; GRA = Green River Airport; N51 = New Area 51; RRR = Ruby Ranch Road; KB = Klondike Bluffs; LV = Long Valley; URR = Utahraptor Ridge; YCR = Yellow Cat Road; PS = Poison Strip; ODR = Owl Draw Road.

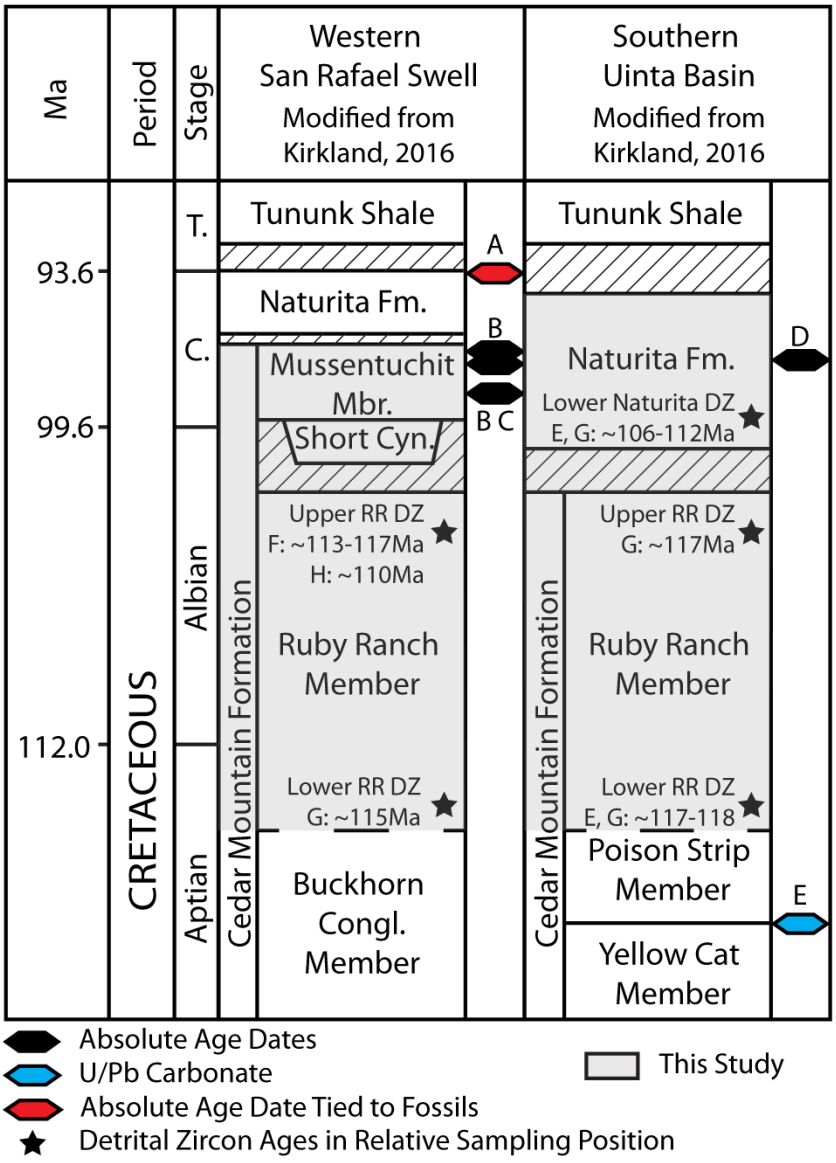

Fig. 2. Stratigraphic columns with absolute and detrital zircon ages. Absolute ages are matched to the timescale at the left. Detrital ages are indicated in their relative sampling position in the stratigraphic column. A: Cobban *et al.* (2006); B: Garrison *et al.* (2007); C: Cifelli *et al.* (1997); D: Barclay *et al.* (2015); E: Ludvigson *et al.* (2010); F: Burton *et al.* (2006); G: Mori (2009); H: Tucker *et al.* (2020).

DeCelles & Giles, 1996; DeCelles & Currie, 1996; Currie, 1997). The overall geometry of the basal deposits of the Cedar Mountain Formation (Buckhorn Conglomerate, Yellow Cat Member and Poison Strip Member) differ from the younger deposits because they thicken in the opposite direction (east; Fig. 3). There are two competing hypotheses to explain this geometry. One model suggests that there was a Late Jurassic/Early Cretaceous foredeep to the west of the study area with a coeval forebulge and backbulge in the study area (Royse, 1993; Currie, 2002; DeCelles, 2004). Basal deposits of the Cedar Mountain Formation in the study area thicken eastward into the backbulge depozone whilst coeval foredeep deposits are missing due to erosion west of the study area. An alternative hypothesis suggests that subduction-related isostatic and dynamic topography in the absence of a developed foreland basin accounts for an eastward thickening of these deposits (Heller & Paola, 1989; Heller *et al.*, 2003; Hunt *et al.*, 2011). This latter model removes the need for the erosion of thick foredeep deposits west of the study area. In either case, the basal Cedar Mountain Formation deposits can be considered separately from the overlying units (Ruby Ranch Member, Mussentuchit Member and Naturita Formation) which are part of a younger foreland basin system. This study deals with these upper Cedar Mountain and Naturita Formation deposits.

The Ruby Ranch Member is the only unit that spans the whole field area. It overlies the Buckhorn Conglomerate on the San Rafael Swell and overlies the Poison Strip Member from Green River, Utah, eastward. The unit is dominantly mudstone with sandstone and conglomerate lenses throughout. Sandstone and conglomerate lenses are interpreted by most authors to have been deposited by low sinuosity or meandering-anastomosed streams (e.g. Young, 1973; Harris, 1980; Currie, 1997; Masters *et al.*, 2004; Sorensen, 2011; Nuse, 2015; Hayden *et al.*, 2019; Cardenas *et al.*, 2020). Detrital zircon maximum depositional ages range from 104 to 118 Ma for the unit (Burton *et al.*, 2006; Mori, 2009; Ludvigson *et al.*, 2010; Chure *et al.*, 2010; Tucker *et al.*, 2020) indicating that it should be no older than Late Aptian and spans the Albian stage (Fig. 2).

The Mussentuchit Member overlies the Ruby Ranch Member on the western side of the San Rafael Swell. The two members are separated by a localized conglomerate which has been informally named the Short Canyon Conglomerate (Doelling & Kuehne, 2013). The Mussentuchit Member consists of sandstone and conglomeratic lenses encased in floodplain mudstones similar to the Ruby Ranch Member. However, the Mussentuchit Member contains more smectitic clay and is significantly more carbonaceous than the Ruby Ranch Member. Sandstones and conglomerates of the unit were deposited by meandering streams (Sorensen, 2011). Radiometric ages exist for the Mussentuchit Member from 96.7 ± 0.5 to 98.39 ± 0.07 Ma (Cifelli *et al.*, 1997; Cifelli & Madsen, 1999; Garrison *et al.*, 2007) which indicate a Cenomanian age (Fig. 2). These ages are similar to those reported for the Naturita Formation in eastern Utah (97.95 + 0.037/−0.12 to 97.601 + 0.049/−0.13 Ma; Barclay *et al.*, 2015; Fig. 2) and the Mowry Shale in Wyoming (97.2 ± 0.7 Ma, 98.5 ± 0.5 Ma; Obradovich, 1993) supporting the idea that the Mussentuchit Member is laterally equivalent to the Naturita Formation of eastern Utah (Sorensen, 2011). For this reason, fluvial deposits of the Mussentuchit Member (western part of the study area) and Naturita Formation (eastern part of the study area) will be considered as one contemporaneous system/unit throughout the remainder of this paper, simply termed 'MN' (Fig. 3).

The Cedar Mountain Formation is overlain by the Naturita Formation. The Naturita Formation records the flooding of the Western Interior Seaway and is a transitional package composed of fluvial, tide-dominated estuarine and marine shoreface deposits (Hunt *et al.*, 1953; Young, 1960, 1973; Peterson & Ryder, 1975; Ryer, 1983; Eaton *et al.*, 1990; Kirschbaum & Schenk, 2010; Antia & Fielding, 2011; Sprinkel *et al.*, 2012; Phillips *et al.*, 2020). The Naturita Formation of the San Rafael Swell (western part of the study area) is composed of tide-dominated estuarine deposits that overlie tidally-influenced fluvial deposits (Phillips *et al.*, 2020). These western Naturita Formation deposits are not considered in this paper. The fully marine Tununk Shale Member of the Mancos Shale (Gilbert, 1877;

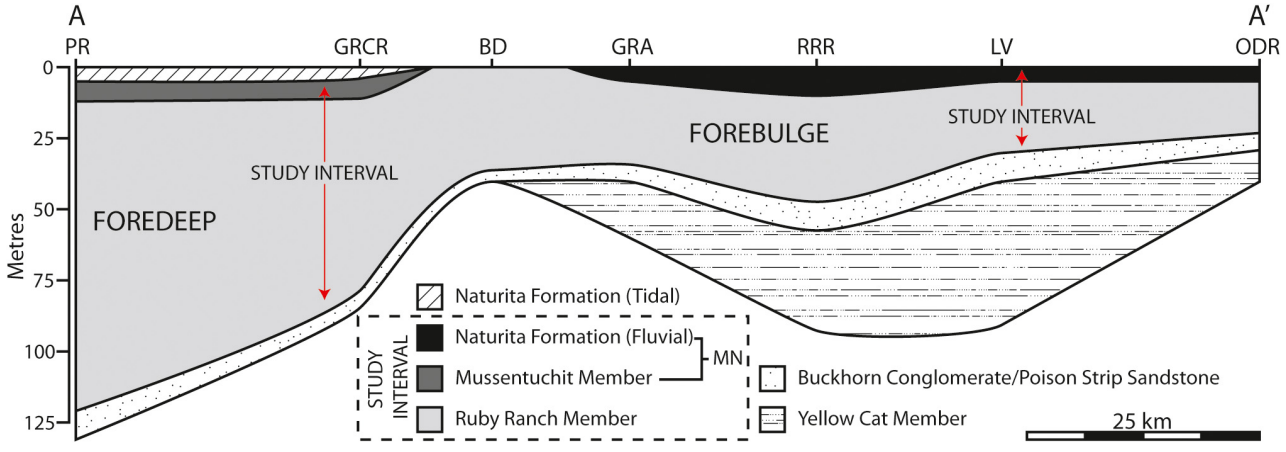

Fig. 3. Cross-section that spans the foredeep to forebulge transition showing the geometry of units. Notice the westward thickening of the study interval into the foredeep and the accompanying thinning onto the forebulge. See Fig. 1 caption for abbreviation definitions.

Stokes, 1944; Kirkland *et al.*, 1997) overlies the Naturita Formation and records the complete flooding of the study area.

METHODS

Field-based

To understand the variety and architecture of fluvial deposits within the study interval, field data were collected at 24 locations. Data collected includes: photographs (all locations), measured sections (15 locations), virtual outcrops (14 locations; Buckley *et al.*, 2008) and palaeocurrent measurements (12 locations, 2138 measurements). Palaeocurrent measurements were evaluated using rose diagrams created with Stereonet 10 (Allmendinger, 2020). Virtual outcrops were generated using photogrammetry on *ca* 23 000 images collected using a Phantom 4 Pro UAV (DJI, Shenzhen, China) and were interpreted in LIME (Buckley *et al.*, 2019) to map the vertical and lateral architectural element organization. Virtual outcrop datasets were used to measure the maximum width and thickness ($n = 135$) of bar elements. Bar thickness is used in subsequent palaeohydraulic calculations.

Satellite imagery

Due to the low structural dips and predominance of heavily weathered mudstone, the study interval contains over 100 examples of exceptionally well-exposed channel belts of both single and multi-storey architectures that can be observed in plan-view (e.g. Williams *et al.*, 2009; Hayden *et al.*, 2019). Channel belts are commonly exposed as caprocks of sinuous ridges. Analysis of satellite data (Google Earth®) coupled with palaeocurrent measurements taken in the field allow recognition of a range of channel sinuosity and planform. Where possible, measurements of maximum width ($n = 104$), radius of curvature ($n = 23$), sinuosity ($n = 27$) and distance from the contemporaneous thrust ($n = 104$) were made. Because channel belts have undergone various amounts of erosion, width measurements are taken at the position where they enter the subsurface (Fig. 4). In cases where such a location does not exist, width measurements are excluded from the analysis, however, sinuosity and radius of curvature were still measured where possible. In many cases, channel belts are stacked and portions of more than one channel belt may be exposed in plan-view (Williams *et al.*, 2007; Nuse, 2015; Hayden *et al.*, 2019; Cardenas *et al.*, 2020). In these situations, the apparent channel belt width measurements may be slightly overestimated and the final width measurement actually represents the total width of stacked channel belts.

FACIES AND ARCHITECTURAL ANALYSIS

Eleven facies have been identified and are grouped into two broad facies associations: FA1 – floodplain; and FA2 – fluvial channel (Tables 1 and 2). Photographs of selected facies are presented in Fig. 5. This section presents detailed descriptions of each facies association with subsequent interpretations.

Facies Association 1 (FA1) – Floodplain

Description

FA1 deposits are composed of varicoloured and/or mottled mudstone, nodular and bedded carbonate (Fig. 5A and B), and thin (<1 m) sandstone sheets (Fig. 5C). Bedded carbonate is laterally continuous for up to a few kilometres and is often scoured through and overlain by sandstone or conglomerate lenses of FA2. Carbonate nodules are present throughout the Ruby Ranch Member of the Cedar Mountain Formation that form distinct and laterally continuous zones (kilometre-scale; Fig. 5A). Septarian nodules are common and some nodules have a botryoidal texture. Nodules are often crudely aligned in vertical columns. Thin sandstone beds (<1 m) are present, these commonly appear massive, but can have ripple cross-lamination or trough cross-stratification. Their lateral continuity can be more than 1 km, although beds are commonly covered by mudstone from above. These beds tend to be fine-grained with a distinct lack of coarser sediment. They often pinch out in both directions, but can sometimes be seen merging with deposits of FA2.

Interpretation

These deposits are interpreted collectively as deposits common to floodplain environments (Kirkland *et al.*, 1997). The dominant lithology is mudstone, and mottled beds are interpreted to represent palaeosols. Where carbonate nodules

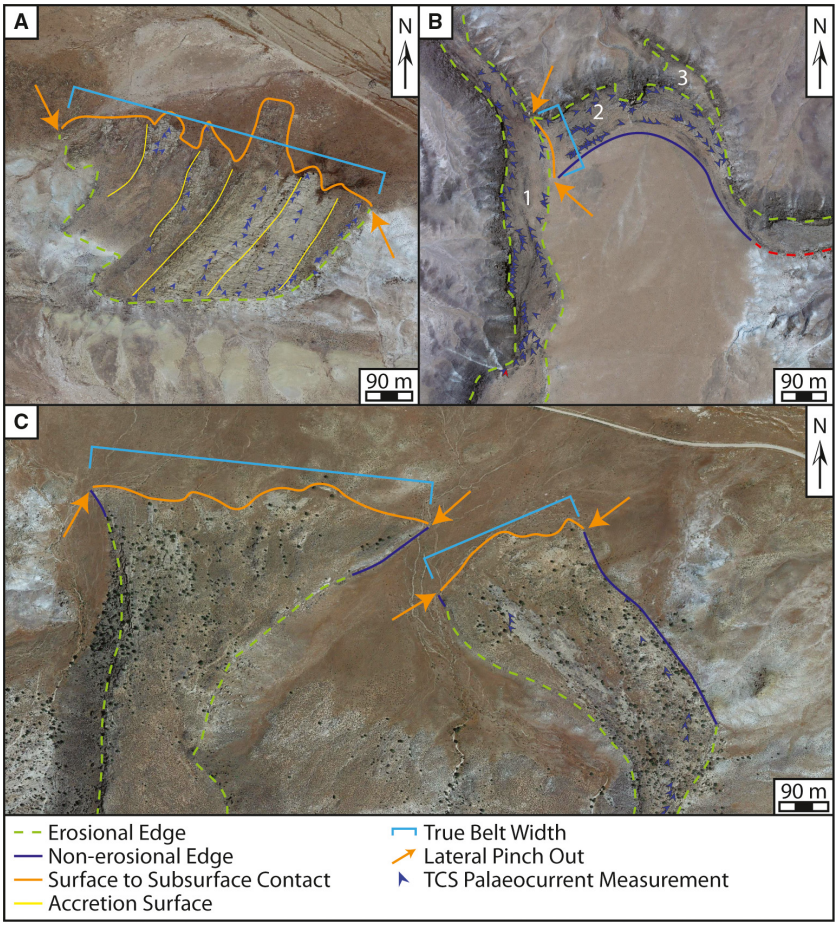

Fig. 4. Three examples of low to moderate sinuosity channel belts within the Cedar Mountain Formation illustrating how channel belt width measurements were taken (Google Earth®). Measurements of channel belt width (blue brackets) are taken where the channel belt enters the subsurface when such a location exists. Orange arrows indicate the lateral pinch-out of channel belts. (A) Plan-view image of a channel belt in the MN interval. This channel belt is single-storey, isolated, and accretion surfaces can be seen in satellite imagery. Accretion direction is to the east. (B) Plan-view image of three narrow channel belts in the Ruby Ranch Member. Channel belt 1 nowhere preserves the true channel belt width due to erosion. The true width of channel belt 2 can only be measured where it passes under channel belt 1 because both margins of the channel can be seen. These contacts were verified in the field. Note that the true width of belt 2 is greater than any other location along the ridge. Channel belt 3 passes under channel belt 2, but the channel margins are difficult to ascertain in satellite imagery. (C) Plan-view image of two channel belts in the MN interval where they enter the subsurface. The two belts are at different stratigraphic levels. Note that the true width of each belt is greater than any other location along the ridge. TCS = trough cross-stratification.

are present forming laterally continuous beds, these are interpreted to be caliche horizons and are an indication of a relatively dry climate (Kirkland *et al.*, 1997). Laterally continuous primary carbonate beds are interpreted to be lake deposits (Montgomery, 2014). Thin sandstone beds are interpreted to be crevasse splay deposits or levées; an interpretation bolstered by the fact that they often merge laterally with fluvial channel deposits, although the possibility exists for terminal splays.

Facies Association 2 (FA2) – Fluvial channels

Description

The composition of FA2 deposits is highly variable (fine sand through to cobble clasts of intrabasinal and extrabasinal origin; Hunt *et al.*, 2011; Fig. 6) and typically poorly sorted (Figs 5D to F, 5H and 6). The conglomerate is composed of well-rounded extrabasinal chert, quartzite and carbonate clasts, and well-rounded to lath shaped intrabasinal mudstone clasts. The dominant

Table 1. Facies in the Cedar Mountain Formation.

Facies code	Facies name	Sedimentary structures, textures and additional notes	Bedding	Facies association
E1	Trough cross-stratified extrabasinal conglomerate	Trough cross-stratification; often poorly cemented; granule to cobble with fine to medium matrix; rounded to subangular; a continuum exists from clast-supported with a sandstone matrix to pebbles present as lags at the base of channels, at the base of individual cross-beds, or as foresets alternating with sandstone; poorly sorted	Thin – very thick	FA2
E2	Massive extrabasinal conglomerate	Massive; well-cemented; granule to cobble with fine to medium matrix; clast-supported; rounded to subangular; poorly sorted	Thin – medium	FA2
I1	Intrabasinal conglomerate	Trough cross-stratification; poorly cemented; entire beds can be composed of calcrete nodules of pebble to cobble size with a fine-grained matrix or calcrete nodules can form a basal lag; poorly sorted	Medium – very thick	FA2
Ss1	Trough cross-stratified sandstone	Trough cross-stratification; soft-sediment deformation; variable cementation; fine to very coarse; well-sorted when fine-grained, poorly to very poorly sorted as maximum grain size increases	Medium – thick	FA1, FA2
Ss2	Current ripple cross-stratified sandstone	Ripple cross-stratification; climbing ripples; variable cementation; fine; well-sorted	Thin – medium	FA1, FA2
Ss3	Planar laminated sandstone	Planar lamination; variable cementation; fine to medium; moderately well-sorted	Medium – thick	FA2
Ss4	Bioturbated or rooted sandstone	Bioturbation: vertical and horizontal tubes with no lining, internal fill is usually the same as the host rock, downward tapering chambered burrows; rooting: downward branching root traces with concentric rings in cross-section; variable cementation; speroidal weathering; fine to medium; well to poorly sorted	Medium – thick	FA1, FA2
Ss5	Massive sandstone	Massive; recessive; spheroidal weathering; fine; well-sorted	Thin – thick	FA1, FA2
M	Mudstone	Massive; varicoloured (white, pale pink, red, purple); mottled; nodular or chippy	Very Thick	FA1
C	Calcrete	Carbonate nodules; pebble to cobble in size; vertical organization; nodules can have a botryoidal texture	Medium – very thick	FA1
D	Dolomite	Silty, bedded dolomite	Medium	FA1

sedimentary structure in all deposits is trough cross-stratification (Figs 5D to F, 5H and 6). Significant planar cross-stratification and ripple cross-lamination may be present locally (Fig. 5I and J). Burrows consist of vertical and horizontal tubes (some meniscate) or funnel shaped, chambered networks concentrated on the upper surfaces of sandstone bodies, and rarely conglomeratic bodies (Fig. 5K). The burrow fill may be identical to the host rock or completely different in colour and/or grain size. Basal and internal lag deposits are common (Fig. 6) and usually contain chert pebbles and carbonate nodules (Fig. 5L). Nodules are similar in appearance to laterally adjacent and underlying nodules in the surrounding mudstone of FA1 (Fig. 6). Although infrequent, carbonate nodules can be the main clast type in deposits of this facies association (Fig. 5H). In most cases, FA2 deposits commonly overlie decimetre to metre-scale beds of nodular carbonate (Figs 5A and 6H).

Facies Association 2 deposits contain distinct master bedding surfaces that have a dip direction that is roughly perpendicular to structures

Table 2. Facies associations in the Cedar Mountain Formation.

Facies association code	Facies association name	Associated facies	Characteristics	Depositional setting
FA1	Floodplain	M – Mudstone C – Calcrete D – Dolomite Ss1 – Trough cross-stratified sandstone Ss2 – Current ripple cross-stratified sandstone Ss4 – Bioturbated or rooted sandstone	Dominantly recessive deposits with some thin ledge forming sandstone or carbonate	Floodplain (floodplain fines, minor lacustrine deposits, crevasse splays)
FA2	Fluvial Channel	E1 – Trough cross-stratified extrabasinal conglomerate E2 – Massive extrabasinal conglomerate I1 – Intrabasinal conglomerate Ss1 – Trough cross-stratified sandstone Ss2 – Current ripple cross-stratified sandstone Ss3 – Planar laminated sandstone Ss4 – Bioturbated or rooted sandstone Ss5 – Massive sandstone M – Mudstone	Channel deposits; lateral accretion dominates over forward accretion; master bedding surfaces are arcuate and are visible on satellite imagery; lensoidal in cross-section with dipping accretion surfaces	Fluvial channel belts

indicative of palaeoflow such as cross-strata, ripples and primary current lineation. In plan-view, master bedding surfaces are arcuate, and palaeocurrent measurements are typically parallel to the trend of each accretion surface at any given point along the arc (Figs 7 and 8).

There is often a distinct alternation of grain sizes forming bedsets of conglomerate followed by bedsets of sandstone in a repeating pattern (Fig. 7). Conglomerate bedsets tend to be recessive and can be completely obscured in plan-view leaving the intervening sandstone intervals as pronounced arcuate ridges. In cross-section view, these conglomerate intervals are exposed and the sandstone–conglomerate–sandstone–conglomerate pattern is clearly visible (Fig. 7). Deposits have a lensoidal geometry and overlie scoured surfaces.

Interpretation

These deposits are interpreted to be the product of migrating fluvial channels within channel belts (Hayden *et al.*, 2019). Master bedding surfaces that dip perpendicular to palaeoflow structures are interpreted as lateral accretion surfaces. Due to the dominance of lateral accretion surfaces and the arcuate nature of those surfaces, the authors interpret these deposits to represent laterally accreting bars of migrating channels (Sorensen, 2011; Hayden *et al.*, 2019; e.g. Figs 7 and 8). Master bedding surfaces that dip in the same direction as palaeoflow structures were not observed here, although this type of accretion has been documented by other workers (e.g. Nuse, 2015; Cardenas *et al.*, 2020). Palaeocurrent measurements indicate that fluvial systems flowed axially (north-eastward) in the foreland basin, and this trend does not vary significantly between the distal foredeep region and forebulge region (Fig. 1). The presence of pebble to cobble sized sediment is indicative of high flow velocities. Burrows, located preferentially on the upper surfaces of these bars, are evidence of colonization of the bar by plant and insect life after the active channel has continued to migrate or had avulsed. Funnel shaped, chambered burrows may be the remains of burrowed root systems or networks created by colonial organisms such as termites or bees (Elliott & Nations, 1998). The secondary carbonate nodules are interpreted to be

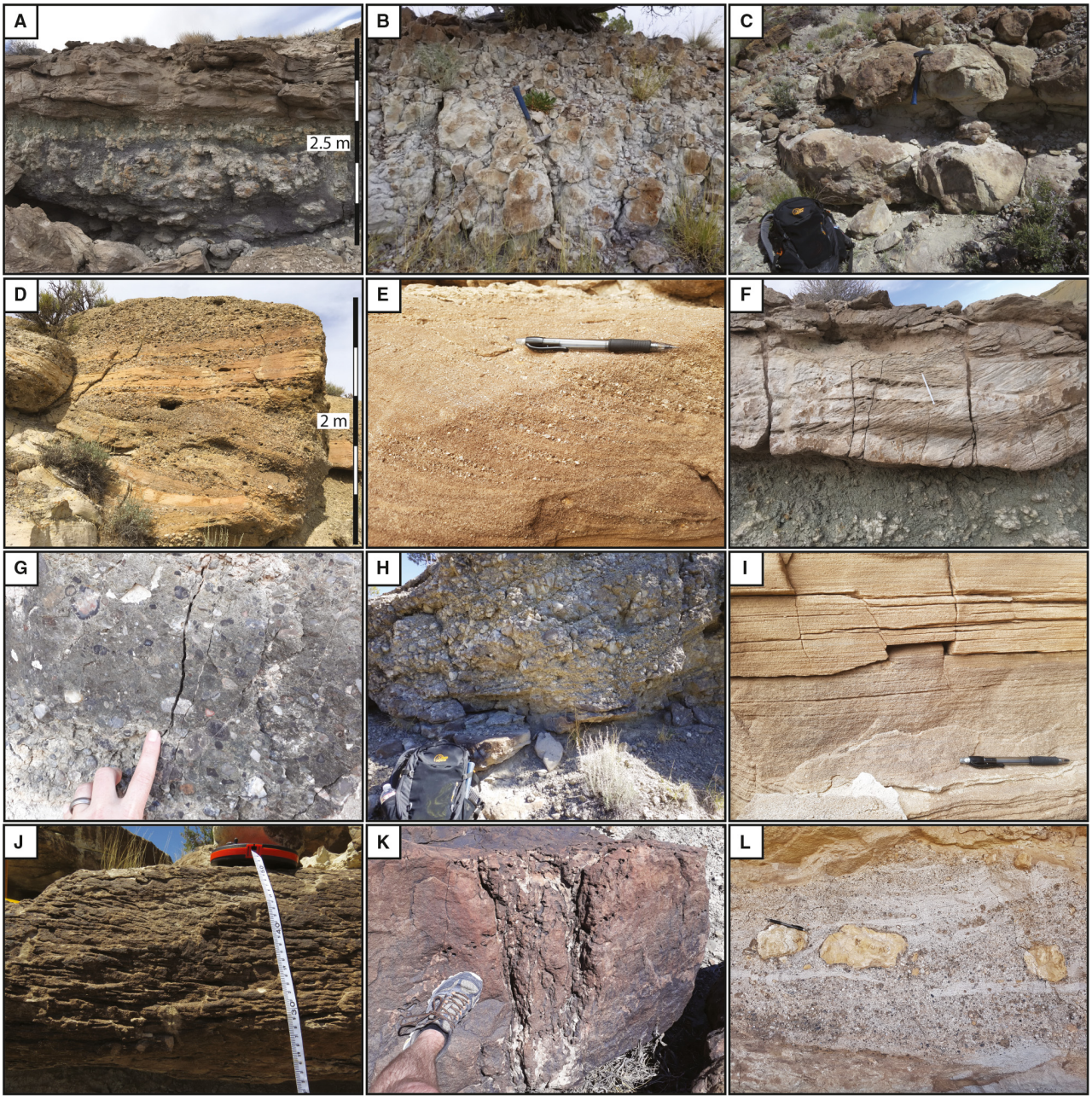

Fig. 5. Common facies in the study interval. (A) Trough cross-stratified sandstone overlying well-developed caliche soil. (B) Dolomite. Hammer for scale (33 cm long). (C) Massive sandstone. Backpack for scale (50 cm tall). (D) Poorly sorted trough cross-stratified extrabasinal conglomerate of pebble size. (E) Poorly sorted trough cross-stratified conglomerate of granule to pebble size. Pencil for scale (*ca* 15 cm long). (F) Trough cross-stratified sandstone. Pen for scale (*ca* 15 cm long). (G) Massive extrabasinal conglomerate. Finger for scale. (H) Intrabasinal trough cross-stratified conglomerate. Clasts are dominantly caliche nodules. Backpack for scale. (I) Planar laminated sandstone. Pencil for scale. (J) Ripple cross-stratified sandstone. Tape is in centimetres. (K) Chambered burrows in sandstone. Note that the downward tapering burrows may indicate colonization of root systems. Foot for scale. (L) Basal lag with cobble sized caliche clasts. Pencil for scale.

sourced from caliche beds below and adjacent to the active channel. The fact that many FA2 deposits commonly sit above a significant caliche bed suggests that the caliche beds may limit the depth to which a channel may easily scour (Maxson, 2011; Figs 5A, 6E and 6H) although the inclusion

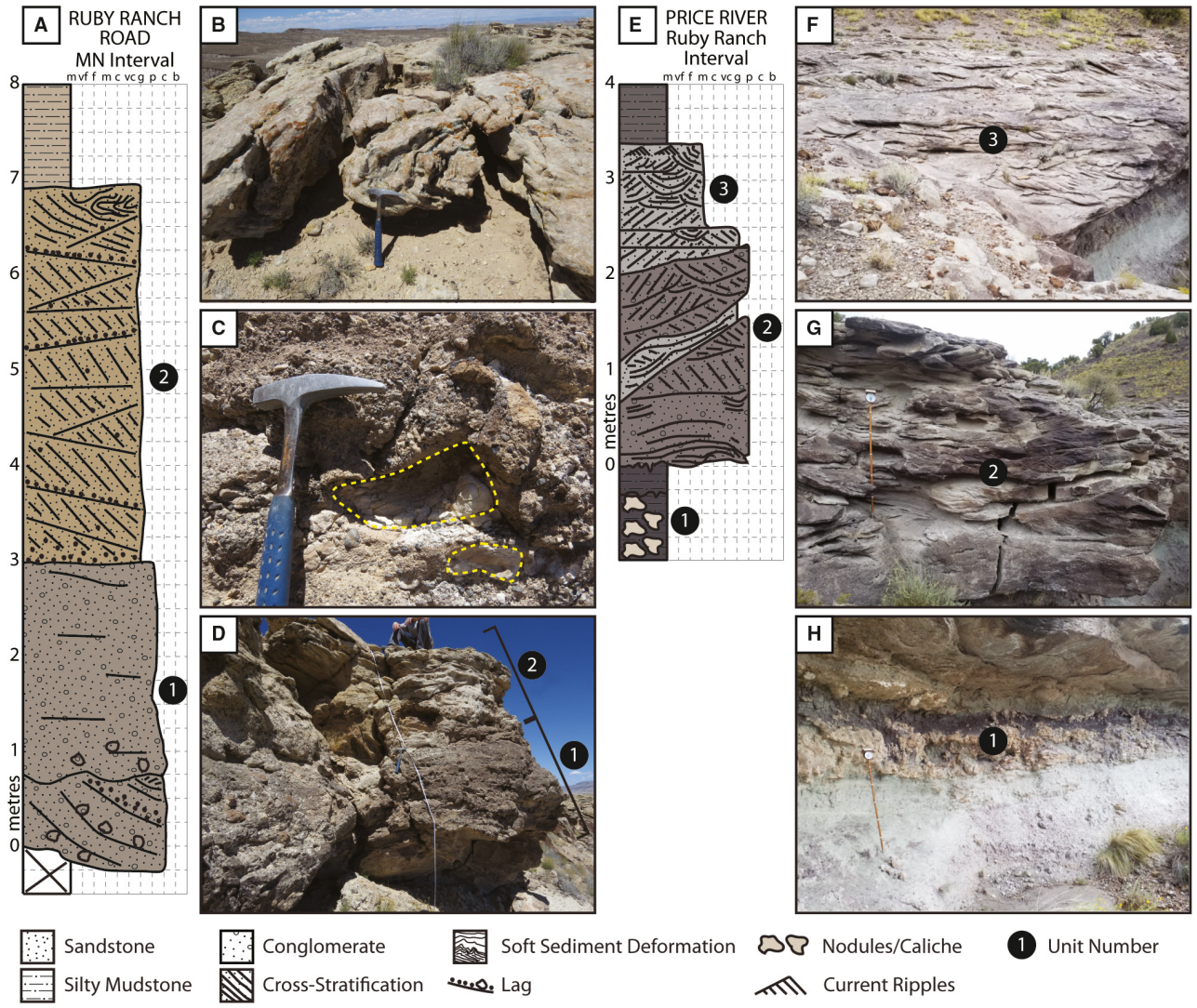

Fig. 6. Representative stratigraphic logs for the MN and Ruby Ranch Intervals. (A) Stratigraphic log through the MN interval from the Ruby Ranch Road locality (RRR). Note that the location name is Ruby Ranch Road but the stratigraphic log is not part of the Ruby Ranch Member. Numbers are shown to match the log to the outcrop photograph in (D). (B) Soft-sediment deformation in the upper part of 'unit 2'. Hammer for scale. (C) Basal lag in 'unit 1'. Cobble size clasts of mudstone are circled in yellow. Hammer for scale (33 cm long). (D) Photograph of the outcrop showing the different 'units'. Numbers on the outcrop are matched to the stratigraphic log in (A). Hammer for scale. (E) Stratigraphic log through a channel body of the Ruby Ranch interval from Price River (PR). Numbers are shown to match the log to the outcrop photographs (F) to (H). (F) Photograph of the upper portion of the logged outcrop. No scale is present, but the unit is approximately 1 m thick. (G) Photograph of the lower portion of the logged outcrop. Staff divisions are in decimetres. (H) Photograph of caliche at the channel base. Staff divisions are in decimetres. Numbers on the outcrop photographs are matched to the stratigraphic log in (E).

of nodules in lag deposits indicates that they are commonly incorporated during channel scour (Fig. 5L).

Architecture

Both single storey ($n = 101$) and multi-storey ($n = 34$) channel bodies are common (Fig. 9). Multi-storey channel bodies are composed of vertically stacked bars in narrow channel belts (median widths of 108.7 m for the MN interval and 220.5 m for the Ruby Ranch interval; Fig. 9A to D). Channel belts have a limited lateral extent when outcrop is perpendicular to palaeoflow direction (Fig. 9A and B). They can, however, extend for more than 1 km when outcrop

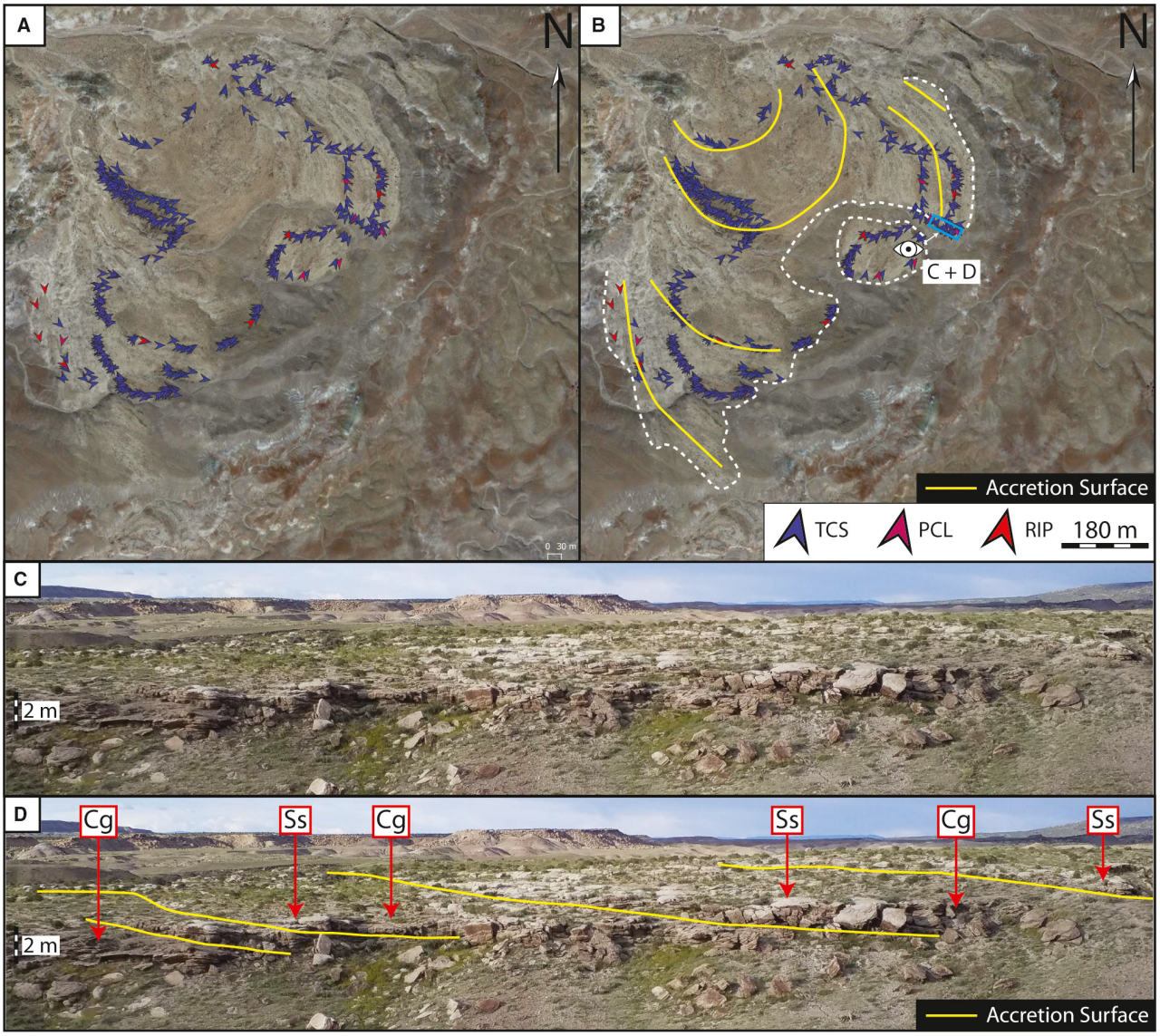

Fig. 7. Satellite image (Google Earth®) and photographs of a point bar element from the MN interval (Location CH). (A) Uninterpreted satellite view of point bar element. (B) Satellite view of point bar element showing arcuate master bedding surfaces with superimposed palaeocurrent measurements. Eye symbol indicates vantage point for the photographs in (C) and (D) (blue box). (C) Uninterpreted flow-perpendicular view of bar. (D) Flow-perpendicular view of bar showing lateral accretion and an alternation between sandstone (Ss) and conglomerate (Cg). Conglomerate is recessive and is only seen in side-view. TCS = trough cross-stratification; PCL = primary current lineation; RIP = ripples.

is parallel to palaeoflow (Fig. 9C and D). Satellite views of exhumed channel belts reveal narrow sinuous bodies (Fig. 4) that extend for up to 8 km in length. All channel bodies, including multi-storey channel bodies, are encased within floodplain deposits (FA1). The dominance of vertically stacked channel belts over laterally amalgamated channel belts, as well as abundant overbank fines, suggests an aggradational system (Posamentier & Vail, 1988; Shanley & McCabe, 1991; Currie, 1997). Percent sandstone is very low (10 to 23%; Fig. 10). There is no change in architectural organization between the Ruby Ranch and MN intervals (Fig. 9).

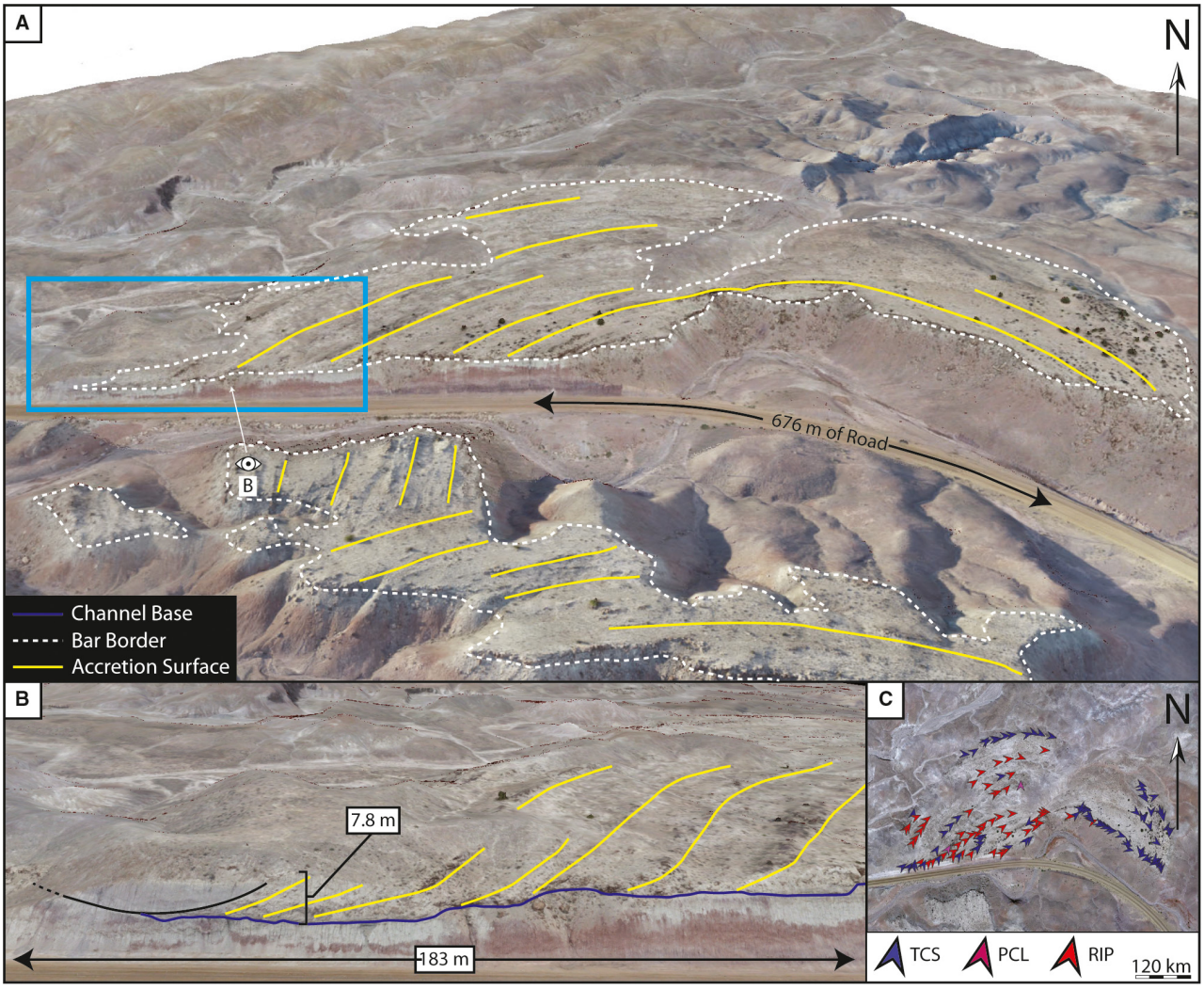

Fig. 8. Virtual outcrop images (no vertical exaggeration) of a channel belt in the Ruby Ranch Member at the Hadden Holes locality (HH). (A) Virtual outcrop showing two point-bar elements of a Ruby Ranch Member channel belt. Arcuate master bedding surfaces are shown. Eye symbol indicates vantage point for (B) (blue box). (B) Virtual outcrop image of roadcut through a point-bar element. Lateral accretion surfaces are shown and the abandoned channel fill is exposed. (C) Satellite view (Google Earth®) of the same point-bar element showing palaeocurrent measurements. TCS = trough cross-stratification; PCL = primary current lineation; RIP = ripples.

DIMENSIONAL DATA

Dimensional data were collected via virtual outcrop models and satellite imagery. The data sets are different yet complimentary. Data collected from virtual outcrop is predominantly restricted to measurements made on a virtual cliff face (apparent width and actual thickness of bars). Virtual outcrop measurements are used for subsequent palaeohydraulic calculations. The resolution of virtual outcrop imagery is sufficient to identify bounding surfaces and, in most cases, sedimentary structures are also identifiable. Data collected from satellite imagery is of planform features (actual belt width, radius of curvature, sinuosity and trend of channel belt deposits) and is not used in palaeohydraulic calculations.

Virtual outcrop data

Width and thickness values (maximum values) obtained for bar elements in virtual outcrop are presented in Table 3 and in Fig. 11. Due to the

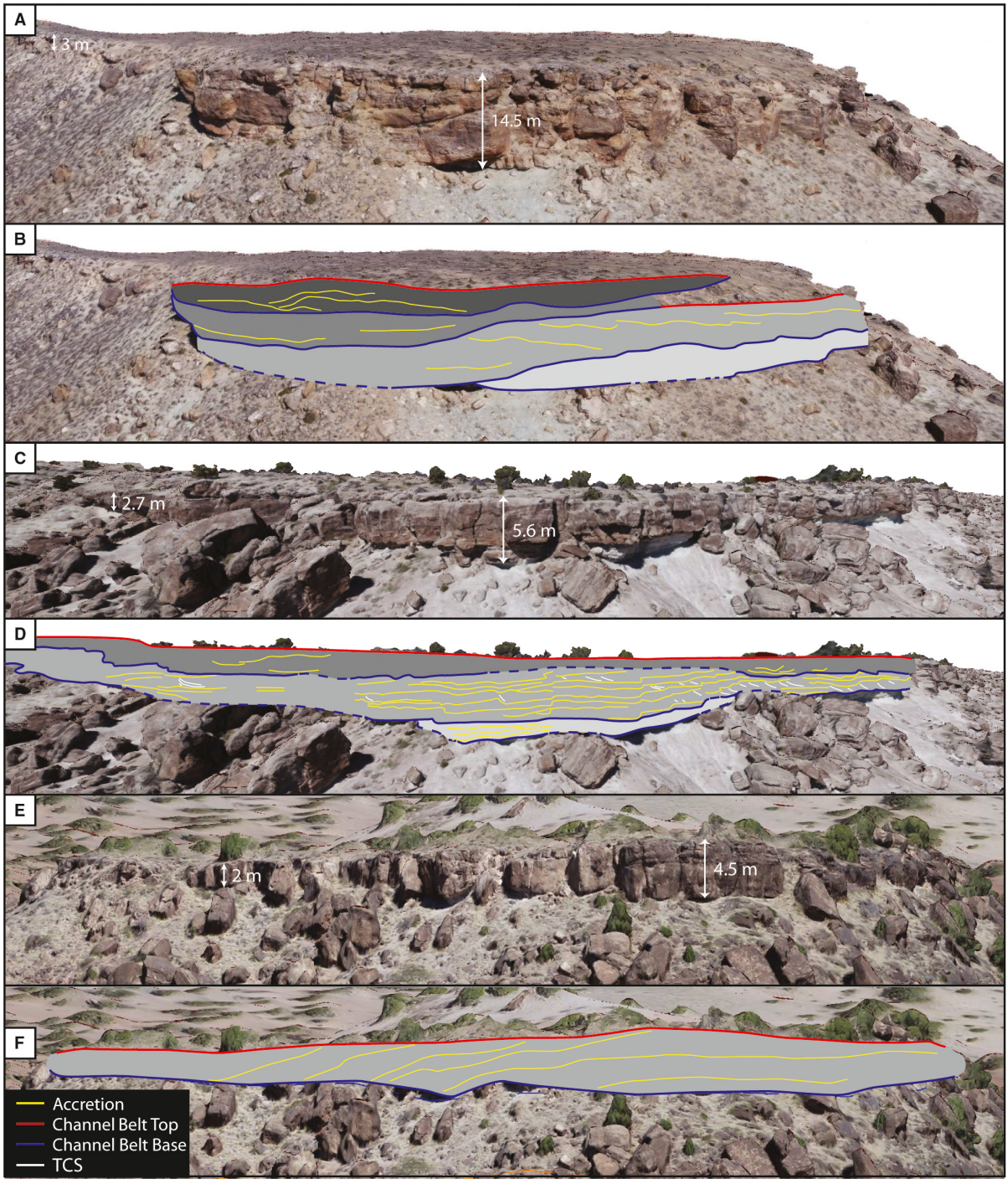

Fig. 9. Architectural styles in the study interval as seen in virtual outcrop models. (A) Uninterpreted virtual outcrop image (no vertical exaggeration) of stacked MN interval channel belts at Utahraptor Ridge (URR). (B) Interpreted version of (A). Outcrop is perpendicular to palaeoflow. Palaeoflow is into the page. The width of the channel belts in the foreground is approximately 135 m. Where the channel belts enter the subsurface (not pictured) there is a maximum width of 370 m. Note that channel belts are stacked vertically. (C) Uninterpreted virtual outcrop image (no vertical exaggeration) of stacked Ruby Ranch Member channel belts at Moore Cutoff Road (MCR). (D) Interpreted version of (C). Outcrop is parallel to palaeoflow. Palaeoflow is to the right and accretion direction is into the page. Note that channel belts are stacked vertically. (E) Uninterpreted virtual outcrop image (1.5× vertical exaggeration) of a Ruby Ranch Member channel belt. (F) Interpreted version of (E). Note the isolated nature of the belt. TCS = trough cross-stratification.

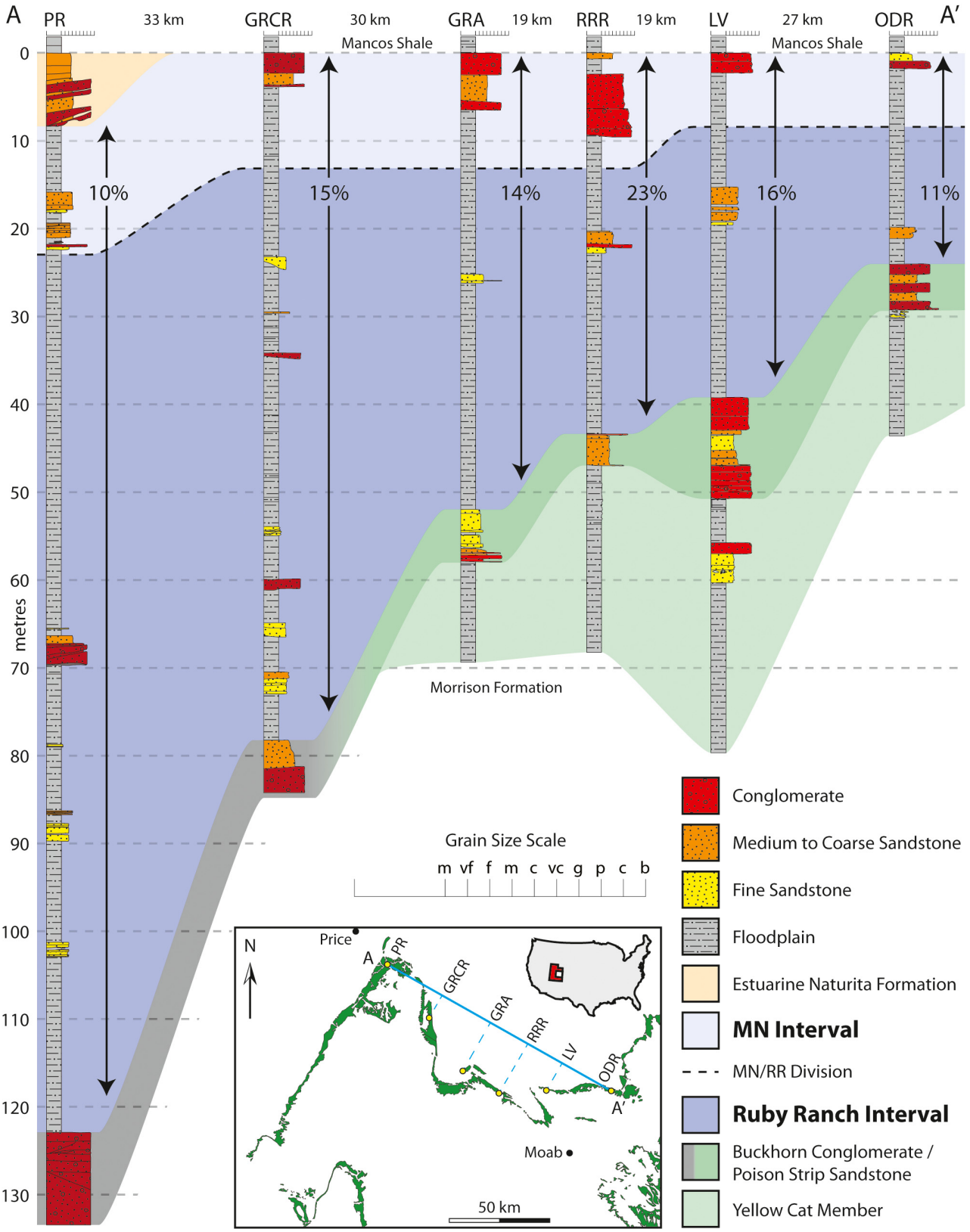

Fig. 10. Cross-section from Price River to Owl Draw Road showing stratigraphic relations for the Cedar Mountain Formation and net to gross values for the target interval. Distance between sections is measured along the projected line of section. See Fig. 1 for abbreviation definitions.

Table 3. Bar element statistics from virtual outcrop (m).

		Bar element width			Bar element thickness			Width/thickness		
Interval	*n*	Min	Med	Max	Min	Med	Max	Min	Med	Max
MN	20	64.5	220.5	1058.4	1.3	3.6	12.2	12.9	64.4	211.7
Ruby Ranch	115	16.9	108.7	1009.4	0.1	1.9	6.4	4.6	64.8	586.6

large number of virtual outcrop models and even larger number of channel belts, accretion direction cannot be interpreted for all bar elements, and it is likely that the dataset contains thickness values for both point bar elements and downstream accreting bar elements. Apparent width has been corrected to true width using mean palaeocurrent values for the region (west or east). To show the range of possible widths, corrections using palaeocurrent values of one standard deviation from the mean are also shown (Fabuel-Perez *et al.*, 2009; Table 3). There is an increase in median width from 49.3 m in the Ruby Ranch to 126.7 m in the MN interval (corrected using mean palaeocurrents), although the range of measurements overlaps considerably

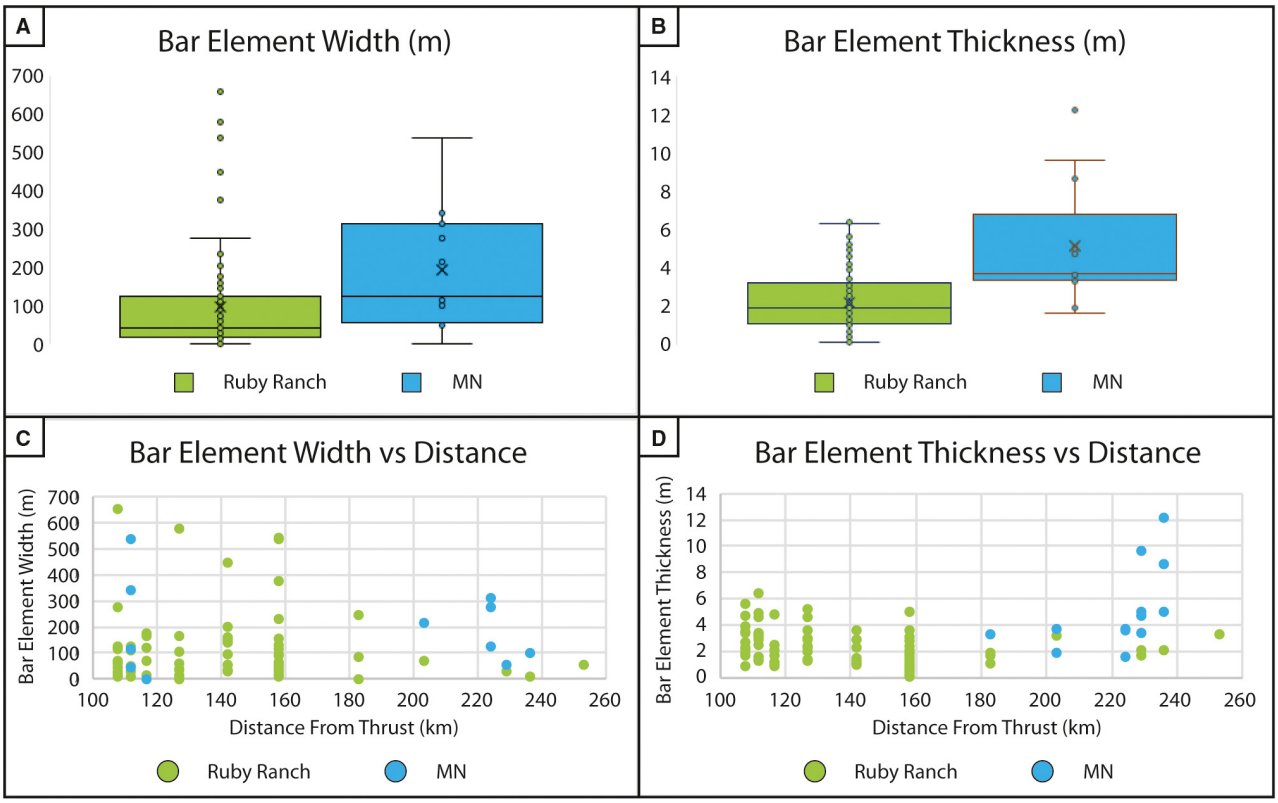

Fig. 11. Plots of dimensional data from virtual outcrop measurements. (A) Box and whisker plots for bar element width. Note the increase in median width for the MN interval. (B) Box and whisker plots for bar element thickness. Note the increase in median thickness for the MN interval. (C) Plot of apparent bar element width versus distance from the thrust front. Note that a similar range exists across the study area. Measurements from a single virtual outcrop model are given the same distance value resulting in many values 'stacked' at a given distance from the thrust belt. (D) Plot of bar element thickness versus distance from the thrust front. Note that channel thickness is consistently less than 7 m across the foredeep to forebulge transition with only a few exceptions. These exceptions are likely trunk rivers for the MN interval and are grouped in the eastern part of the study area.

(Fig. 11A). Thickness measurements are robust and indicate an increase from 1.9 m in the Ruby Ranch to 3.6 m in the MN interval, again with overlap of ranges (Fig. 11B). The thickness outliers are important for palaeohydraulic calculations because they represent the deepest channels preserved in the study area and are interpreted to be deposits of trunk rivers. It should be noted that, while difficult to prove in two-dimensional outcrop exposure, some measurements may represent the outer bend of a point bar which may result in depths greater than true mean depth (Bridge & Mackey, 1993).

To better understand variations in bar element dimensions across the foredeep to forebulge transition, width and thickness have been plotted against distance (Fig. 11C and D) from a datum in central Utah that approximates the position of the palaeothrust front (DeCelles, 2004). Distance measurements were made perpendicular to the trend of the thrust front. All bar elements from a single virtual outcrop are given the same distance value. Most width values are less than 400 m across the field area but maximum widths are higher between 100 km and 160 km from the palaeothrust (Fig. 11C). Most thickness measurements are less than 7 m and an obvious distance variation is not present except for three outliers in the distal portion of the field area (between 220 km and 240 km from the palaeothrust, Fig. 11D).

Satellite data

Statistics for channel belts are presented in Table 4 and Fig. 12. These data show a similar increase in the median width for MN channel belts relative to the underlying Ruby Ranch Member, although the ranges overlap (Fig. 12A). A distance measurement from the palaeothrust front to each channel belt was made to determine if any systematic changes to channel belt width occur across the foredeep to forebulge transition (Fig. 12B). A small anticlinal structure (Woodside Dome) exists on the north-east flank of the larger San Rafael Swell anticline where structural dips are as high as 18°. In this relatively steeply dipping region, planform exposure is extremely limited, resulting in a sampling bias not present to the east and west. Excluding this area, channel belt widths are consistently less than 800 m regardless of distance from the thrust (Fig. 12B). Two outliers exist in the MN interval east of Ruby Ranch Road that are considerably wider than the majority. These channel belts are likely the plan-view expression of trunk rivers. A qualitative trend was taken for each channel belt as a substitute for palaeocurrent data by drawing a straight line along the length of the belt and taking an azimuth measurement. These trend measurements agree well with actual palaeocurrent measurements and indicate a north-easterly flow direction (Fig. 1).

PALAEOHYDRAULICS

The goal of analyzing palaeohydraulics is to evaluate changes in palaeodischarge and palaeodrainage in the Ruby Ranch and MN intervals, and to analyze the possible influence of a backwater effect in the MN interval during the initial stages of marine transgression in the study area. Direct measurement or estimates of channel width and depth are needed to estimate discharge and the backwater effect can be evaluated with an estimate of channel depth, slope and drainage area (Blum *et al.*, 2013).

Estimating palaeodischarge

Point bar element thickness measurements have been made on virtual outcrop models and the thickest for each interval (Ruby Ranch and MN) is taken to represent a trunk river of the system. For an estimation of discharge, cross-sectional area is first calculated by multiplying the palaeochannel depth and width. The thickness of the preserved bar element is estimated to be

Table 4. Channel belt statistics from satellite imagery (m).

	Channel belt width				Radius of curvature				Sinuosity			
Interval	*n*	Min	Med	Max	*n*	Min	Med	Max	*n*	Min	Med	Max
MN	47	35	238	1739	6	73	158	568	5	1.09	1.35	4.90
Ruby Ranch	132	11	80	636	42	62	235	530	41	1.05	1.14	1.93

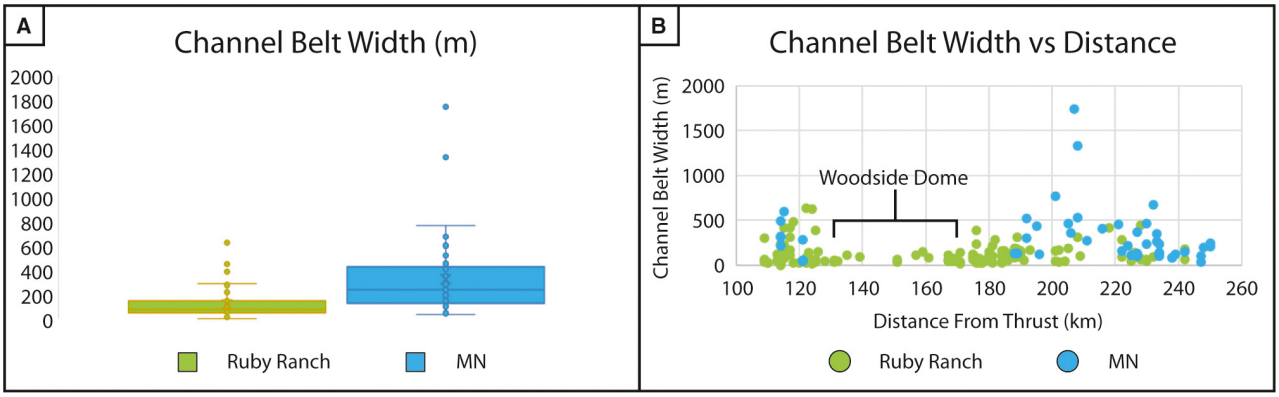

Fig. 12. Dimensional data from satellite imagery. (A) Box and whisker plots of channel belt width. Note the increase in median channel belt width in the MN interval. (B) Plot of channel belt width versus distance from the thrust front. Note that between 130 km and 170 km from the thrust there is a paucity of data. This is due to outcrop quality and steeply dipping beds around Woodside Dome. Excluding this area, values are consistently less than 800 m with few exceptions. The exceptions are likely the plan-view expression of trunk channels.

90% of bankfull channel depth (Bridge & Mackey, 1993; Eq. 1). This correction is used in the calculations as well as an adjustment (0.65) to account for the fact that channels are not rectangular (Bridge & Mackey, 1993; Eq. 2). It is also necessary to account for the fact that bankfull channel depths can be up to three times the mean bankfull depth near bend apices (Bridge & Mackey, 1993). Since point bar deposits are the dominant bar type, mean bankfull depth is estimated from bankfull depth using the equation in Table 5.

Channel width was calculated using empirical relationships reported in Bridge & Mackey (1993) providing a range of estimates (Table 5). The use of a range of estimates is most appropriate due to the natural variability in width observed in modern rivers over very short stretches. This variation in width is illustrated with a modern example from the Texas Gulf Coast with the use of the Global Width Database for Large Rivers (Yamazaki *et al.*, 2019; Fig. 13). The Colorado and Brazos rivers have significant variations in width over their lower stretches (generally between 50 m and 200 m; Fig. 13A). Additionally, significant variation over a 5 km stretch of the Colorado River is documented (over 100 m; Fig 13B).

Mud-filled channels in the study interval are very rare. An example of a mud-filled channel is present at the Hadden Holes locality (HH, Fig. 1) that is visible along a road cut (Fig. 8B). The mud plug is not fully preserved but its width is estimated to be approximately 50 m. Estimates for channel width derived from empirical relationships are between 67 m and 92 m for this channel. These estimates are not a perfect match at 17 to 42 m wider than the preserved channel width. However, these values are significantly less than the natural variability observed in the Colorado and Brazos rivers.

Velocity is estimated for a given channel depth from a phase diagram for medium sand of Rubin & McCulloch (1980). The use of this plot assumes that peak discharge in a channel is accompanied by the formation of dunes, which may not always be true. However, dunes were the primary bedform, as indicated by the dominance of trough cross-stratification in all channel deposits, and a range of velocities helps to minimize this issue. The ranges of possible velocities for each interval are shown in Fig. 14A. To determine a lower bound on possible discharge for each system, the minimum velocity from the phase diagram and the minimum width estimate are used (Table 5). Similarly, to determine an upper bound on possible discharge, the maximum velocity and width estimates are used (Table 5). Discharge is calculated using Eq. 3:

$$d_b = h/0.9 \quad \text{Bridge \& Mackey, 1993} \tag{1}$$

$$A = d_b * w_c * 0.65 \quad \text{Bhattacharya \& MacEachern, 2009} \tag{2}$$

$$Q = U * A \tag{3}$$

where d_b is bankfull channel depth, h is preserved bar thickness, w_c is channel width, A is

Table 5. Palaeohydraulic estimations for thickest point bar deposits from virtual outcrop.

Interval	Bar thickness (m)	Bankfull channel depth (m)	Mean channel depth (m)	Width estimate (m); Crane (1982)	Width estimate (m); Bridge & Mackey (1993)	Width estimate (m); Bridge & Mackey (1993)	Minimum bankfull discharge (m^3/s)	Maximum bankfull discharge (m^3/s)	Slope for minimum discharge; Gardner (1983)	Slope for maximum discharge; Gardner (1983)
Ruby Ranch	6.4	7.1	4.1	118.7	113.4	144.7	314.5	1023.1	0.00035	0.00026
MN	12.2	13.6	7.7	331.0	366.9	400.9	1895.6	5269.6	0.00022	0.00017
$w_c = 12.82 * d_b^{1.59}$		Crane (1982)			d_m to d_b conversion:					
$w_c = 8.88 * d_m^{1.82}$		Bridge & Mackey (1993)			$d_m = d_b * 0.57$		Bridge & Mackey (1993)			
$w_c = 15.85 * d_m^{1.58}$		Bridge & Mackey (1993)								

cross-sectional area, U is velocity and Q is discharge.

Palaeohydraulics have previously been estimated for two channel belts near the SWGR location (Fig. 1) in the Ruby Ranch Member (Williams *et al.*, 2009). These calculations were based on inverted channel dimensions with an aim to better constrain palaeohydraulics for similar inverted channel deposits on Mars. Important to these calculations is the assumption that caprock ridges of the Cedar Mountain Formation represent river channels and not channel belts.

A subsequent analysis was performed on five channel belts in the same location (Hayden *et al.*, 2019). Hayden *et al.* (2019) interpret the caprock ridges as the remnants of channel belts rather than single channel deposits and used physics-based methods rather than empirical relationships in palaeohydraulic calculations. The Hayden *et al.* (2019) estimates of discharge ranged from 240 to 850 m^3/s for bars of 1.8 to 2.5 m thick. The estimates herein are calculated with a maximum bar thickness of 6.4 m resulting in a higher range of discharge (315 to 1023 m^3/s) from the same stratigraphic interval.

Estimating drainage area

A positive correlation exists between bankfull discharge and drainage area (Matthai, 1990; Mulder & Syvitski, 1995; Davidson & Hartley, 2010; Blum *et al.*, 2013). A similar relationship exists between point bar thickness and drainage area. These relationships are used to estimate drainage area from the calculated range of discharges for each interval (Fig. 14B and C). The Ruby Ranch and MN intervals plot as rivers with 10^4 km^2 and 10^5 km^2 scale drainage, respectively [see Eel-scale and Colorado-scale (TX) rivers; Fig. 14D].

Estimating backwater length

Backwater length is inversely correlated with river slope (Blum *et al.*, 2013; Fig. 14D). With estimates of discharge, slope (S) can be estimated using an empirical relationship (Lane, 1957; Gardner, 1983; Eq. 4):

$$S = 0.00146 * Q^{-0.25} \quad \text{Gardner, 1983} \tag{4}$$

Using the inverse relationship presented by Blum *et al.* (2013; Fig. 14D), the potential for backwater effects in the MN interval can be

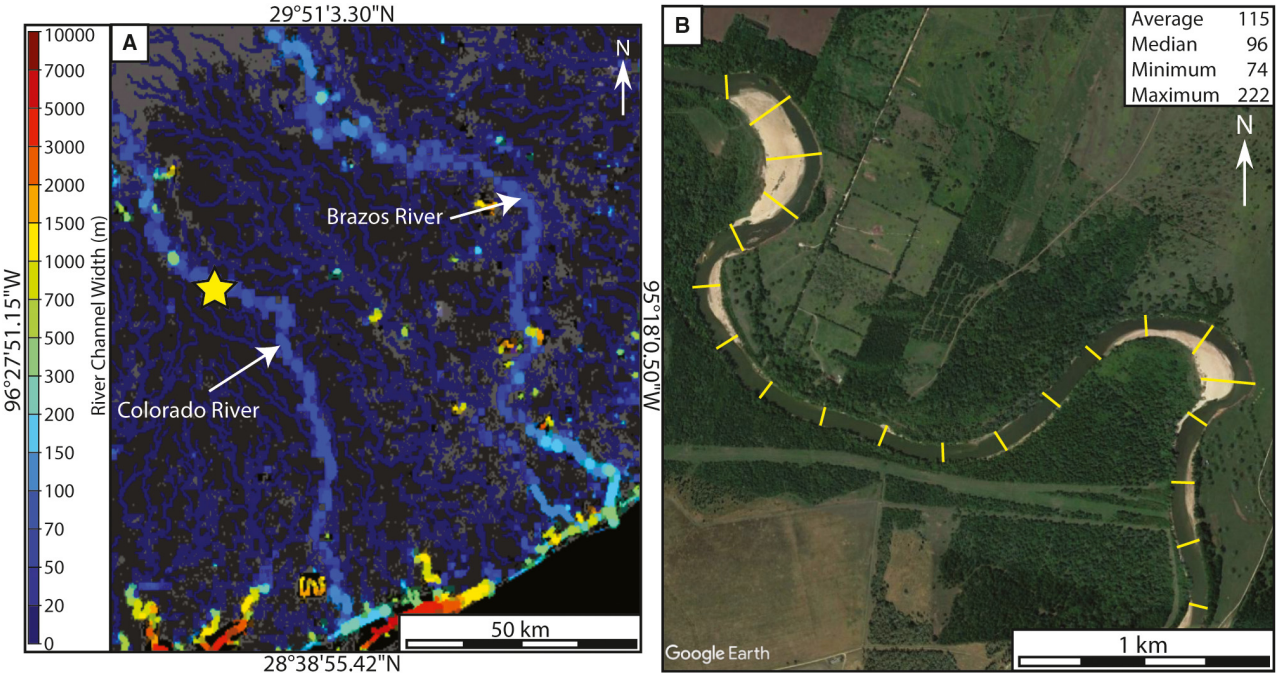

Fig. 13. Analysis of channel width for Gulf coast rivers. (A) Map of channel width derived from the Global Width Database for Large Rivers (Yamazaki *et al.*, 2019). Bright spots (>200 m) along the course of each river result from near channel lakes or ponds. Additionally, bright areas near the shoreline represent lagoonal or estuarine regions and should not be confused with fluvial environments. Excluding these areas, typical channel widths are binned between 50 m and 200 m. Star indicates location of (B). (B) Detailed analysis of a 5 km stretch of the Colorado River (TX; Google Earth®; 29°21'35.68″N, 96°16'1.96″W) showing variation in channel width.

evaluated. The MN rivers were 10^5 km^2 scale with a minimum slope of 0.00017 suggesting that an expected backwater length would be less than 70 km. The distance from the trunk river outcrop (Owl Draw Road) to the closest known equivalent shoreface deposit near the Utah–-Colorado state line (Young, 1960, 1973) is between 50 km and 60 km, indicating that backwater effects could be preserved in the MN interval, but would likely be minimal.

DISCUSSION

Climate change and drainage capture

As established previously, channels increase in width and depth over time (from Ruby Ranch to MN) and result in an associated increase in palaeodischarge estimates. Increased discharge may be the result of enhanced precipitation due to climate change (within the catchment and/or basin), drainage capture, or a combination of the two.

Basin climate

Significant sedimentological evidence for a changing climate in the basin is present in both the Ruby Ranch and MN intervals. The Ruby Ranch Member contains an abundance of caliche soils and a distinct lack of carbonaceous material (Kirkland *et al.*, 1997). Caliche soils are commonly found in semi-arid to arid environments (e.g. Reeves, 1970; Schlesinger, 1985). Conversely, the overlying MN interval lacks caliche soils and contains significant carbonaceous material (Kirkland *et al*, 1997) suggesting a transition from semi-arid or arid climate to a humid climate in the basin.

It is likely that the aridity recorded within the Ruby Ranch Member is the result of a significant rain shadow to the east of the orogenic belt (Elliott *et al.*, 2007; Suarez *et al.*, 2014; Ludvigson *et al.*, 2015). There was a consistent increase in elevation of the orogenic belt throughout Ruby Ranch time and a maintenance of high elevation during MN time which enhanced or maintained a rain shadow in the basin (DeCelles & Coogan, 2006; Elliott *et al.*, 2007; Suarez *et al.*, 2014; Hatzell, 2015; Ludvigson *et al.*, 2015).

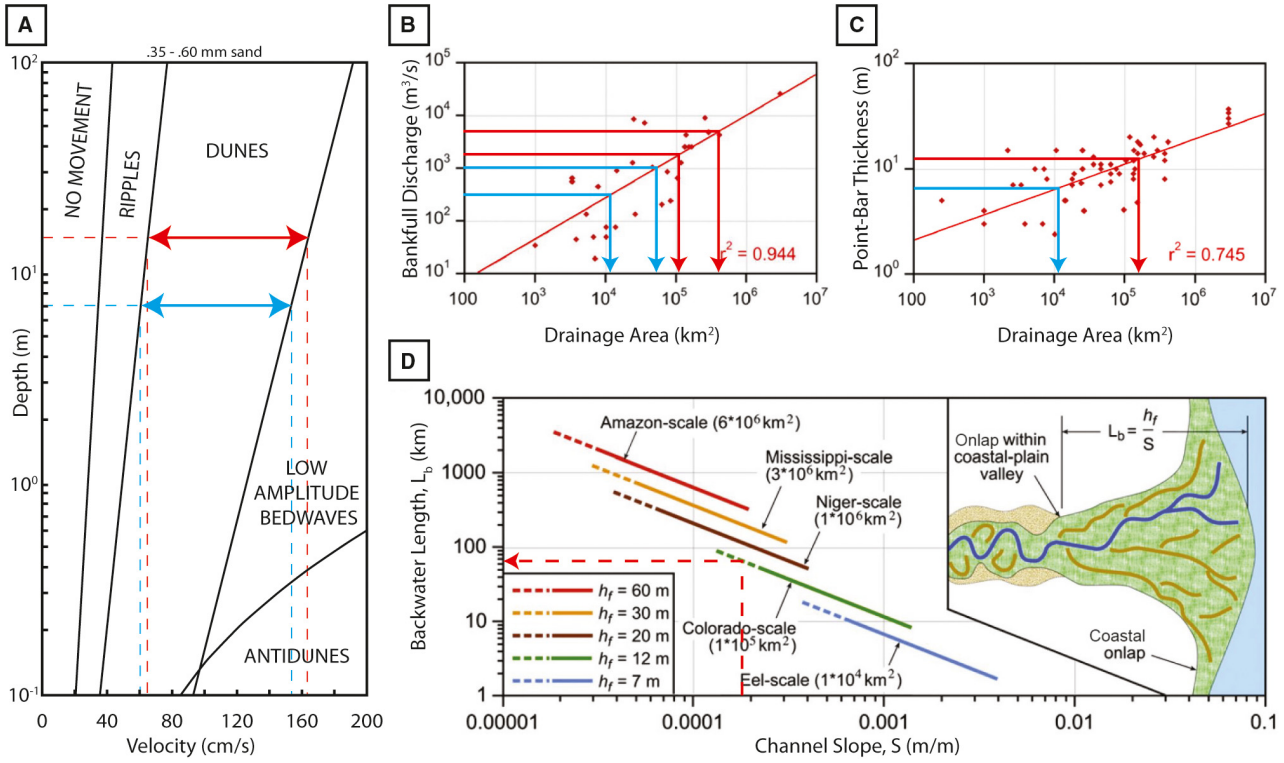

Fig. 14. Various plots from the literature used in palaeohydraulic calculations. (A) Depth-velocity phase diagram for medium sand modified from Rubin & McCulloch (1980) and Bhattacharya & Tye (2004). Velocity ranges for the thickest Ruby Ranch and MN interval bars are shown. (B) and (C) Plots showing the relationship of bankfull discharge or point-bar thickness and drainage area for late Pleistocene to modern single-channel meandering systems modified from Blum *et al.* (2013). Note that in both instances, Ruby Ranch rivers plot as 10^4 km^2 scale and MN interval rivers plot as 10^5 km^2 scale rivers. (D) Plot showing the relationship between backwater length and channel slope modified from Blum *et al.* (2013). For MN rivers which are 10^5 km^2 scale (Colorado scale), a minimum calculated slope of 0.00017 results in a backwater length of 70 km or less.

Several workers have analyzed carbon and oxygen isotopes from bioapatite and pedogenic calcite (Suarez *et al.*, 2014; Hatzell, 2015; Ludvigson *et al.*, 2015). These studies confirm an arid to semi-arid environment within the basin during Ruby Ranch time (Suarez *et al.*, 2014; Hatzell, 2015; Ludvigson *et al.*, 2015) and a time of increased humidity during the MN interval (Suarez *et al.*, 2014; Hatzell, 2015). Hatzell (2015) estimated a mean annual precipitation of 274 or 599 mm/year for the Ruby Ranch Member, and 883 or 910 mm/year for the MN interval (the pairs of estimates being derived from two independent calculations). This increased precipitation for the MN interval is further corroborated by leaf area analysis which provided a mean annual precipitation estimate of 810 mm/year for the MN interval (Arens & Harris, 2015). Suarez *et al.* (2014) suggest that a shift in summer wind direction from westerlies during Ruby Ranch time to easterlies during MN time brought marine moisture into the area from the encroaching Western Interior Seaway (Poulsen *et al.*, 1999). The increased precipitation may have had a substantial impact on discharge rates within the basin, ended the formation of caliche soils, and enhanced plant growth and the preservation of organic matter in the MN interval.

Catchment climate

Unfortunately, little is known about the climate in the catchment. However, Suarez *et al.* (2014) found that some animals living in the basin ingested ^{18}O depleted water that was likely derived from seasonal snowmelt or orographic rainout in the catchment. The Suarez *et al.* (2014) study corroborates the idea that high elevations existed in the catchment (DeCelles & Coogan, 2006; Elliott *et al.*, 2007; Suarez *et al.*, 2014; Hatzell, 2015; Ludvigson *et al.*, 2015). Increasing elevations in the orogenic belt may have enhanced orographic rainfall in the

catchment, resulting in greater discharges to the basin.

Drainage capture

The early history of foreland basin development is dominated by small disconnected drainages (Gupta, 1997; Horton & DeCelles, 2001). As development continues, drainage capture takes place resulting in increased catchment area and discharge (Gupta, 1997; Horton & DeCelles, 2001). Additionally, significant increases in discharge can also occur when rivers flowing away from the foreland basin are captured by rivers flowing into the foreland basin (Koons, 1995). Drainage area increased by an order of magnitude from Ruby Ranch to MN time (Fig. 14). The authors propose that small (10^4 km^2 scale) Ruby Ranch catchments merged to create larger (10^5 km^2 scale) MN rivers. The MN rivers tapped larger areas increasing the relative input from orographic rainfall, thereby increasing discharge in the basin.

Backwater effect

The MN fluvial system is oriented axially in the basin and most of the outcrop belt is oriented perpendicular to the axis of the foreland basin which does not permit evaluation of downstream trends in width and thickness. The only location where downstream changes can be evaluated is along the western flank of the San Rafael Swell. If the backwater effect were present in that region the authors would expect to see narrowing and deepening of channels downstream (i.e. decrease in width to thickness ratio; Blum *et al.*, 2013). Unfortunately, only seven measurements from three locations are available in this region. Width to thickness ratios listed in downstream direction are 19.2 m ($n = 1$) at Mussentuchit Wash, an average of 101.2 m ($n = 4$) at Moore Cutoff Road and an average of 75.1 ($n = 2$) at Hadden Holes (Fig. 1). These measurements show no systematic downstream changes in width to thickness ratios. The authors conclude that there is not sufficient evidence for backwater effects in the field area, but further data is required to definitely establish this.

Fluvial style as a function of foreland basin depozone

The outcrop belt within the study area provides an opportunity to evaluate changes to the fluvial

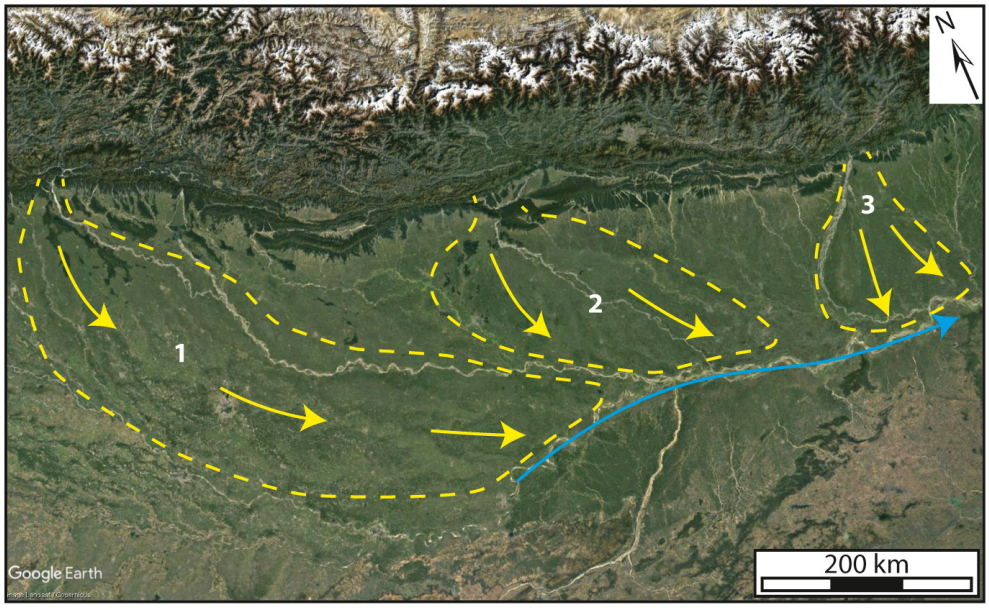

Fig. 15. Distributive fluvial system (DFS) of the Himalayan foreland basin. Note that fan 1 is strongly asymmetrical with an oblique termination at the axial system. Similar ancient fans would be difficult to identify solely based on palaeocurrent measurements due to the similarity in palaeocurrent directions between the distributive and axial systems. Fan 2 is slightly asymmetrical and fan 3 is perpendicular to the axial system. Fans of this type would be easier to identify in the ancient based on palaeocurrent measurements which would show systematic variation in palaeocurrent direction along the termination of the fan with an accompanying abrupt shift in palaeocurrent directions for the axial system. Fan outlines are from Shukla *et al.* (2001).

systems as a function of foreland basin depozone or distance from the thrust. No significant changes in width, thickness or architecture were noted in an area that spans the distal foredeep depozone and the forebulge depozone (Figs 11 and 12). The only notable difference between the two areas is in the overall geometry of the package, with significant thickening into the foredeep (50 m in the forebulge to 1100 m in the foredeep; Currie, 1997; Figs 1 and 3). Synorogenic conglomerates, formed in the proximal foredeep, are preserved outside of the study area in central Utah (Lawton *et al.*, 1997, 2007; Sprinkel *et al.*, 1999).

Modern foreland basins are dominated by distributive fluvial systems (DFS) which terminate at, and are tributary to, axial rivers (e.g. Hartley *et al.*, 2010; Weissmann *et al.*, 2010). Modern examples of DFS in foreland basin settings are the Andean, Himalayan and Alaskan foreland basins (Gupta, 1997; Horton & DeCelles, 2001; Shukla *et al.*, 2001; Hartley *et al.*, 2010; Weissmann *et al.*, 2010) and ancient DFS within foreland basins have also been documented (e.g. Rittersbacher *et al.*, 2014; Owen *et al.*, 2015, 2019; Primm *et al.*, 2018). Deposits of the upper Cedar Mountain Formation have recently been interpreted as a distributive fluvial system (Holmes, 2017; Cardenas *et al.*, 2020). The two most distinctive features of a distributive fluvial system are the presence of an apex and a fan-shaped planform. Proving the presence of an apex is unlikely due to low preservation potential. However, statistical methods have been used successfully in the prediction of an apex (Owen *et al.*, 2015). The preserved outcrop of the study interval is, unfortunately, not wide enough in geographic extent to permit the identification of a fan-shaped planform via palaeocurrent data.

In spite of the absence of an apex and the inability to prove a fan-shaped planform, the upper Cedar Mountain Formation shares several characteristics with distal DFS deposits of sinuous single-thread rivers: channels have limited lateral migration, exhibit lateral displacement by avulsion (Speed *et al.*, 2019; Cardenas *et al.*, 2020), contain vertically stacked channel belts (e.g. Williams *et al.*, 2007; Nuse, 2015; Cardenas *et al.*, 2020) and are encased in significant floodplain deposits (Mohrig *et al.*, 2000; Jerolmack & Mohrig, 2007; Weissmann *et al.*, 2010, 2013, 2015; Davidson *et al.*, 2013; Fig. 10). The increase in channel size from the Ruby Ranch to MN interval may be partly due to progradation of the DFS placing more proximal deposits above more distal deposits. However, the abundance of floodplain fines (Fig. 10) and matching architectural styles indicate a distal DFS position for both the Ruby Ranch and MN intervals, suggesting that the amount of progradation would likely be minor.

A shift in palaeocurrent from the western (70° to 80°) to eastern (30° to 60°) portions of the field area is present (Fig. 1). This shift in palaeocurrent may represent the oblique termination of an asymmetrical DFS at an axial system that existed in eastern Utah and western Colorado. Palaeocurrent information for coeval deposits in Colorado are not available but a strong northerly directed palaeocurrent is present for lower Cedar Mountain Formation deposits (e.g. Craig, 1981; Currie, 1998; Dickinson & Gehrels, 2008; Hunt *et al.*, 2011) and the presence of thick (12.2 m) trunk channel deposits with significant channel depths in the eastern portion of the study area corroborates this interpretation. An asymmetrical DFS would have palaeocurrent directions in the distal regions that are oblique to the axial system (e.g. Shukla *et al.*, 2001). This work documents the existence of asymmetrical DFS planform in the modern Himalayan foreland basin (Fig. 15) and the same feature has been documented in an ancient example from the Bighorn Basin in Wyoming (Owen *et al.*, 2019). The authors agree with recent workers (Holmes, 2017; Cardenas *et al.*, 2020) that the upper Cedar Mountain Formation was likely deposited as a distributive fluvial system based on the presence of several predicted features of a distributive fluvial system listed above, as well as the predominance of these planforms in modern foreland basin settings.

CONCLUSIONS

Ruby Ranch and 'MN' [Mussentuchit Member (western part of the study area) and Naturita Formation (eastern part of the study area)] channel belts exhibit no change in architecture or fluvial style across the distal foredeep to forebulge depozones suggesting that position in the foreland basin does not necessarily have a controlling influence on architecture or fluvial planform. No backwater effect was observed and

base level rise appears to have had no influence on fluvial architecture.

Channels and channel belts of the Ruby Ranch Member of the Cedar Mountain Formation are significantly smaller than the overlying MN interval. Palaeodischarge and palaeodrainage area calculations derived from bar element thicknesses indicate that MN rivers drained an area that was an order of magnitude larger than Ruby Ranch rivers. The increase in discharge over time can be explained by increased precipitation and drainage capture.

Channel belts are narrow, low to moderate sinuosity, aggradationally stacked and are completely encased in mudstone. These features are consistent with, and the studied deposits may represent, the distal portion of an ancient distributive fluvial system.

ACKNOWLEDGEMENTS

This work was funded by the SAFARI group. We are deeply grateful to Joe Phillips, Sean Kelly, James Mullins, Ryan King and Jostein Myking Kjærefjord for help in the field. We would also like to thank Associate Editor, Christopher Fielding, for handling the review of this paper. Additionally we thank reviewers Benjamin Cardenas and Brian Currie for their comments and suggested revisions which have greatly enhanced this paper.

NOMENCLATURE

d_b	Bankfull channel depth
h	Preserved bar thickness
w_c	Channel width
A	Cross-sectional area
U	Velocity
Q	Discharge
S	Slope

DATA AVAILABILITY STATEMENT

The data that support the findings of this study are available from the corresponding author upon reasonable request.

REFERENCES

Allmendinger, R.W. (2020) Stereonet 10, Program for stereographic projection.

Antia, J. and **Fielding, C.R.** (2011) Sequence stratigraphy of a condensed low-accommodation succession: Lower Upper Cretaceous Dakota Sandstone, Henry Mountains, Southeastern Utah. *AAPG Bull.*, **995**, 413–447.

Arens, N.C. and **Harris, E.B.** (2015) Paleoclimatic reconstruction for the Albian-Cenomanian transition based on a dominantly angiosperm flora from the Cedar Mountain Formation, Utah, USA. *Cretac. Res.*, **53**, 140–152.

Barclay, R.S., **Rioux, M.**, **Meyer, L.B.**, **Bowring, S.A.**, **Johnson, K.R.** and **Miller, I.M.** (2015) High precision U-Pb zircon geochronology for Cenomanian Dakota Formation floras in Utah. *Cretac. Res.*, **52**, 213–237.

Bhattacharya, J.P. and **MacEachern, J.A.** (2009) Hyperpycnal rivers and prodeltaic shelves in the Cretaceous Seaway of North America. *J. Sediment. Res.*, **79**, 184–209.

Bhattacharya, J.P. and **Tye, R.S.** (2004) Searching for modern Ferron analogs and application to subsurface interpretation. *Utah Am. Assoc. Pet. Geol. Stud. Geol.*, **50**, 39–57.

Blum, M., **Martin, J.**, **Milliken, K.** and **Garvin, M.** (2013) Paleovalley systems: insights from Quaternary analogs and experiments. *Earth-Sci. Rev.*, **116**, 128–169.

Bridge, J.S. and **Mackey, S.D.** (1993) A theoretical study of fluvial sandstone body dimensions. *Int. Assoc. Sedimentol. Spec. Publ.*, **15**, 213–236.

Buckley, S.J., **Howell, J.A.**, **Enge, H.D.** and **Kurz, T.H.** (2008) Terrestrial laser scanning in geology: data acquisition, processing and accuracy considerations. *J. Geol. Soc. Lond.*, **165**, 625–638.

Buckley, S.J., **Ringdal, K.**, **Naumann, N.**, **Dolva, B.**, **Kurz, T.H.**, **Howell, J.A.** and **Dewez, T.J.B.** (2019) LIME: software for 3-D visualization, interpretation, and communication of virtual geoscience models. *Geosphere*, **15**, 222–235.

Burton, D., **Greenhalgh, B.W.**, **Britt, B.B.**, **Kowallis, B.J.**, **Elliott, W.S.** and **Barrick, R.** (2006) New radiometric ages from the Cedar Mountain Formation, Utah and the Cloverly Formation, Wyoming: implications for contained dinosaur faunas. *Geol. Soc. Am. Abstracts Programs*, **38**, 52.

Cardenas, B.T., **Mohrig, D.**, **Goudge, T.A.**, **Hughes, C.M.**, **Levy, J.S.**, **Swanson, T.**, **Mason, J.** and **Zhao, F.** (2020) The anatomy of exhumed river-channel belts: bedform to belt-scale river kinematics of the Ruby Ranch Member, Cretaceous Cedar Mountain Formation, Utah, USA. *Sedimentology*, **67**, 3655–3682.

Chure, D., **Britt, B.B.**, **Whitlock, J.A.** and **Wilson, J.A.** (2010) First complete sauropod dinosaur skull from the Cretaceous of the Americas and the evolution of sauropod dentition. *Naturwissenschaften*, **97**, 379–391.

Cifelli, R.L., **Kirkland, J.I.**, **Weil, A.**, **Deino, A.L.** and **Kowallis, B.J.** (1997) High-precision $^{40}Ar/^{39}Ar$ geochronology and the advent of North America's Late Cretaceous terrestrial fauna. *Proc. Natl. Acad. Sci. U.S.A.*, **94**, 11163–11167.

Cifelli, R.L. and **Madsen, S.K.** (1999) *Spalacotheriid symmetrodonts* (Mammalia) from the medial cretaceous (upper Albian or lower Cenomanian) Mussentuchit local fauna—Cedar Mountain Formation, Utah, USA. *Geodiversitas*, **21**, 167–214.

Cobban, W., **Walaszczyk, I.**, **Obradovich, J.D.** and **McKinney, K.C.** (2006) A USGS zonal table for the upper cretaceous middle Cenomanian–Maastrichtian of the Western Interior of the United States based on ammonites, inoceramids, and radiometric ages. *USGS Ofr*, **2006–1250**, 50.

Craig, L.C. (1981) Lower Cretaceous rocks, southwestern Colorado and southeastern Utah. In: *Geol. Parad. basin Rocky Mtn. Assoc. Geol. Guid. 1981 F. Conf*, pp. 195–200.

Crane, R.C. (1982) A computer model for the architecture of avulsion controlled alluvial suites: Thesis, University of Reading, 534 p.

Currie, B.S. (1997) Sequence stratigraphy of nonmarine Jurassic-Cretaceous rocks, central Cordilleran foreland-basin system. *Bull. Geol. Soc. Am.*, **109**, 1206–1222.

Currie, B.S. (1998) Upper Jurassic-Lower Cretaceous Morrison and Cedar Mountain formations, NE Utah-NW Colorado; relationships between nonmarine deposition and early Cordilleran foreland-basin development. *J. Sediment. Res.*, **68**, 632–652.

Currie, B.S. (2002) Structural configuration of the Early Cretaceous Cordilleran foreland-basin system and Sevier thrust belt, Utah and Colorado. *J. Geol.*, **110**, 697–718.

Currie, B.S., **McPherson, M.L.**, **Dark, J.P.** and **Pierson, J.S.** (2008) Reservoir characterization of the Cretaceous Cedar Mountain and Dakota Formations, southern Uinta Basin, Utah: year-two report. *Utah Geol. Surv. Open File Rep.*, **516**, 116.

Currie, B.S., **McPherson, M.L.**, **Hokanson, W.**, **Pierson, J.S.** and **Homan, M.B.** (2012) Reservoir characterization of the lower Cretaceous Cedar Mountain and Dakota Formations, Northern Uinta Basin, Utah. *Utah Geol. Surv. Open File Rep.*, **597**, 39.

Davidson, S.K. and **Hartley, A.J.** (2010) Towards a quantitative method for estimating paleohydrology from clast size and comparison with modern rivers. *J. Sediment. Res.*, **80**, 688–702.

Davidson, S.K., **Hartley, A.J.**, **Weissmann, G.S.**, **Nichols, G.J.** and **Scuderi, L.A.** (2013) Geomorphic elements on modern distributive fluvial systems. *Geomorphology*, **180–181**, 82–95.

DeCelles, P.G. (2004) American Journal of Science Late Jurassic to Eocene evolution of the Cordilleran thrust belt and foreland basin system, western U.S.A. *Am. J. Sci.*, **304**, 105–168.

DeCelles, P.G. and **Coogan, J.C.** (2006) Regional structure and kinematic history of the Sevier fold-and-thrust belt, central Utah. *Bull. Geol. Soc. Am.*, **118**, 841–864.

DeCelles, P.G. and **Currie, B.S.** (1996) Long-term sediment accumulation in the Middle Jurassic-early Eocene Cordilleran retroarc foreland-basin system. *Geology*, **24**, 591–594.

DeCelles, P.G. and **Giles, K.N.** (1996) Foreland basin systems. *Basin Res.*, **8**, 105–123.

Dickinson, W.R. and **Gehrels, G.E.** (2008) Sediment delivery to the Cordilleran foreland basin: insights from U-Pb ages of detrital zircons in Upper Jurassic and Cretaceous strata of the Colorado Plateau. *Am. J. Sci.*, **308**, 1041–1082.

Doelling, H.H. and **Kuehne, P.A.** (2013) *Geologic Map of the Short Canyon Quadrangle, Emery County*, 31 p., 2 plates. Utah Geol. Surv. Map 255DM, Utah.

Eaton, J.G., **Kirkland, J.I.** and **Kauffman, E.G.** (1990) Evidence and dating of Mid-Cretaceous tectonic activity in the San Rafael Swell, Emery County. *Utah. Mt. Geol.*, **27**, 39–45.

Elliott, D.K. and **Nations, J.D.** (1998) Bee burrows in the Late Cretaceous (Late Cenomanian) Dakota Formation, northeastern Arizona. *Ichnos*, **5**, 243–253.

Elliott, W.S., **Suttner, L.J.** and **Pratt, L.M.** (2007) Tectonically induced climate and its control on the distribution of depositional systems in a continental foreland basin, Cloverly and Lakota Formations (Lower Cretaceous) of Wyoming, U.S.A. *Sediment. Geol.*, **202**, 730–753.

Fabuel-Perez, I., **Hodgetts, D.** and **Redfern, J.** (2009) A new approach for outcrop characterization and geostatistical analysis of a low-sinuosity fluvial-dominated succession using digital outcrop models: upper Triassic Oukaimeden Sandstone Formation, central high Atlas, Morocco. *Am. Assoc. Pet. Geol. Bull.*, **93**, 795–827.

Gardner, T.W. (1983) Paleohydrology and paleomorphology of a Carboniferous, meandering, fluvial sandstone. *J. Sediment. Petrol.*, **53**, 991–1005.

Garrison, J.R., **Brinkman, D.**, **Nichols, D.J.**, **Layer, P.**, **Burge, D.** and **Thayn, D.** (2007) A multidisciplinary study of the Lower Cretaceous Cedar Mountain Formation, Mussentuchit Wash, Utah: a determination of the paleoenvironment and paleoecology of the *Eolambia caroljonesa* dinosaur quarry. *Cretac. Res.*, **28**, 461–494.

Gilbert, G.K. (1877) *Report on the Geology of the Henry Mountains*, pp. 212. Government Printing Office, Washington DC.

Gupta, S. (1997) Himalayan drainage patterns and the origin of fluvial megafans in the Ganges foreland basin. *Geology*, **25**, 11–14.

Harris, D.R. (1980) Exhumed paleochannels in the Lower Cretaceous Cedar Mountain Formation near Green River, Utah. *Brigham Young Univ. Geol. Stud.*, **27**, 51–66.

Hartley, A.J., **Weissmann, G.S.**, **Nichols, G.J.** and **Warwick, G.L.** (2010) Large distributive fluvial systems: characteristics, distribution, and controls on development. *J. Sediment. Res.*, **80**, 167–183.

Hatzell, G.A. (2015) Paleoclimate implications from stable isotope analysis of sedimentary organic carbon and vertebrate fossils from the Cedar Mountain Formation, Utah, U.S.A. M.S. thesis, Fayetteville, University of Arkansas, 54 pp.

Hayden, A.T., **Lamb, M.P.**, **Fischer, W.W.**, **Ewing, R.C.**, **McElroy, B.J.** and **Williams, R.M.E.** (2019) Formation of sinuous ridges by inversion of river-channel belts in Utah, USA, with implications for Mars. *Icarus*, **332**, 92–110.

Heller, P.L., **Dueker, K.** and **McMillan, M.E.** (2003) Post-Paleozoic alluvial gravel transport as evidence of continental tilting in the U.S. Cordillera. *Bull. Geol. Soc. Am.*, **115**, 1122–1132.

Heller, P.L. and **Paola, C.** (1989) The paradox of Lower Cretaceous gravels and the initiation of thrusting in the Sevier orogenic belt, United States Western Interior. *Geol. Soc. Am. Bull.*, **101**, 864–875.

Holmes, A.D. (2017) Sedimentology and taphonomy of the *Abydosaurus mcintoshi*quarry, (Naturita Formation, Early Cretaceous, Latest Albian), Dinosaur National Monument, Utah. MS Thesis, Brigham Young University, Provo, Utah, 60 pp.

Horton, B.K. and **DeCelles, P.G.** (2001) Modern and ancient fluvial megafans in the foreland basin system of the central Andes, southern Bolivia: implications for drainage network evolution in fold-thrust belts. *Basin Res.*, **13**, 43–63.

Hunt, C.B., **Averitt, P.** and **Miller, R.L.** (1953) Geology and geography of the Henry Mountains region, Utah. *US Geol. Surv. Prof. Pap.*, **228**, 234.

Hunt, G.J., **Lawton, T.F.** and **Kirkland, J.I.** (2011) Detrital zircon U-Pb geochronological provenance of Lower Cretaceous strata, foreland basin, Utah. *Utah Geol. Assoc. Publ.*, **40**, 193–211.

Jerolmack, D.J. and **Mohrig, D.** (2007) Conditions for branching in depositional rivers. *Geology*, **35**, 463–466.

Kirkland, J.I., **Britt, B.**, **Burge, D.L.**, **Carpenter, K.**, **Cifelli, R.**, **DeCourten, F.**, **Eaton, J.**, **Hasiotis, S.** and **Lawton, T.** (1997) Lower to middle cretaceous dinosaur faunas of the central Colorado plateau: a key to understanding 35 million years of tectonics, sedimentology, evolution and biogeography. *Brigham Young Univ. Geol. Stud.*, **42**, 69–103.

Kirkland, J.I., **Cifelli, R.L.**, **Britt, B.B.**, **Burge, D.L.**, **DeCourten, F.L.**, **Eaton, J.G.** and **Parrish, J.M.** (1999) Distribution of vertebrate faunas in the Cedar Mountain Formation, east-central Utah. *Misc. Publ. Utah Geol. Surv.*, **99**, 201–217.

Kirkland, J.I., **Suarez, M.**, **Suarez, C.** and **Hunt-Foster, R.** (2016) The Lower Cretaceous in east-central Utah—The Cedar Mountain Formation and its bounding strata. *Geol. Intermt. West*, **3**, 101–228.

Kirschbaum, M. and **Schenk, C.J.**(2010) Sedimentology and reservoir heterogeneity of a valley-fill deposit–a field guide to the Dakota Sandstone of the San Rafael Swell, Utah. *U.S. Geol. Surv. Sci. Investig. Rep., Sci.*, **36**.

Koons, P.O. (1995) Modeling the topographic evolution of collisional belts. *Annu. Rev. Earth Planet. Sci.*, **23**, 375–408.

Lane, E.W. (1957) A study of the shape of channels formed by natural streams flowing in erodible material. U.S. Army Corps of Engineers. Missouri River Div., Omaha, Nebraska, Sediment Studies Program, 9, 106 pp.**

Lawton, T.F., **Sprinkel, D.A.**, **DeCelles, P.G.**, **Mitra, G.**, **Sussman, A.J.** and **Weiss, M.P.** (1997) Stratigraphy and structure of the Sevier thrust belt and proximal foreland-basin system in central Utah: A transect from the Sevier Desert to the Wasatch Plateau. *Brigham Young Univ. Geol. Stud.*, **42**, 33–67.

Lawton, T.F., **Sprinkel, D.A.** and **Waanders, G.L.** (2007) The Cretaceous Canyon Range Conglomerate, central Utah—stratigraphy, structure and significance, *in* Willis, G.C., Hylland, M.D., Clark, D.L., and Chidsey, T.C., Jr., editors, Central Utah—Diverse Geology of a Dynamic Landscape. *Utah Geol. Assoc. Publ.*, **36**, 101–122.

Leopold, L.B. and **Bull, W.A.** (1979) Base level, aggradation and grade. *Proc. Am. Phil. Soc.*, **123**, 168–202.

Ludvigson, G.A., **Joeckel, R.M.**, **Gonzalez, L.A.**, **Gulbranson, E.L.**, **Rasbury, E.T.**, **Hunt, G.J.**, **Kirkland, J.I.** and **Madsen, S.** (2010) Correlation of Aptian-Albian carbon isotope excursions in continental strata of the Cretaceous foreland basin, eastern Utah, U.S.A. *J. Sediment. Res.*, **80**, 955–974.

Ludvigson, G.A., **Joeckel, R.M.**, **Murphy, L.R.**, **Stockli, D.F.**, **González, L.A.**, **Suarez, C.A.**, **Kirkland, J.I.** and **Al-Suwaidi, A.** (2015) The emerging terrestrial record of Aptian-Albian global change. *Cretac. Res.*, **56**, 1–24.

Mackin, J.H. (1948) Concept of the graded river. *Geol. Soc. Am. Bull.*, **59**, 464–511.

Masters, S.L., **Maxson, J.A.** and **Madsen, S.K.** (2004) Anastomosing fluvial system of the Cedar Mountain Formation, eastern Utah—a paleoenvironmental and taphonomic analysis. *Geol. Soc. Am. Abstracts with Programs*, **36**, 60.

Matthai, H.F. (1990) Floods: Surface Water Hydrology. *Geol. Soc. Am.*, **1**, 97–120.

Maxson, J. (2011) Complex interactions between fluvial channels and syn-depositional pedogenic carbonate in the lower Cretaceous Cedar Mountain Formation and Dinosaur National Monument, Utah and Colorado. *Geol. Soc. Am. Abstracts with Programs*, **43**, 2.

Mohrig, D., **Heller, P.L.**, **Paola, C.** and **Lyons, W.J.** (2000) Interpreting avulsion process from ancient alluvial sequences: Guadalope-Matarranya system (northern Spain) and Wasatch Formation (western Colorado). *GSA Bull.*, **112**, 1787–1803.

Montgomery, E. (2014) Limnogeology and chemostratigraphy of carbonates and organic carbon from the Cedar Mountain Formation (CMF), eastern Utah. M.S. thesis, University of Texas at San Antonio, San Antonio, 68 pp.

Mori, H. (2009) Dinosaurian faunas of the Cedar Mountain Formation and LA-ICP-MS detrital zircon ages for three stratigraphic sections. Thesis. Bigham Young University, Provo, Utah, 108 pp.

Mulder, T. and **Syvitski, J.P.M.** (1995) Turbidity currents generated at river mouths during exceptional discharges to the world oceans. *J. Geol.*, **103**, 285–299.

Nuse, B.R. (2015) Flow processes and sedimentation in a low-sinuosity high net-sand content fluvial channel belt: 3D outcrop study of the Cedar Mountain Formation, Utah. Thesis, Colorado School of Mines, Golden, Colorado, 44 pp.

Obradovich, J.D. (1993) A Cretaceous time scale. In: *Evolution of the Western Interior Basin* (Eds Caldwell, W.G.E. and Kauffman, E.G.). *Geol. Soc. Can. Spec. Pap.*, **39**, 379–396.

Owen, A., **Hartley, A.J.**, **Ebinghaus, A.**, **Weissmann, G.S.** and **Santos, M.G.M.** (2019) Basin-scale predictive models of alluvial architecture: constraints from the Palaeocene-Eocene, Bighorn Basin, Wyoming, USA. *Sedimentology*, **66**, 736–763.

Owen, A., **Nichols, G.J.**, **Hartley, A.J.**, **Weissmann, G.S.** and **Scuderi, L.A.** (2015) Quantification of a distributive fluvial system: the Salt Wash DFS of the Morrison Formation, SW USA. *J. Sed. Res.*, **85**, 544–561.

Peterson, F. and **Ryder, R.T.** (1975) Cretaceous rocks in the Henry Mountains region, Utah and their relation to neighboring regions. Canyonlands Ctry. *Four Corners Geol. Soc. 8th F. Conf. Guideb.*, 167–189.

Phillips, S.P., **Howell, J.A.**, **Hartley, A.J.** and **Chmielewska, M.** (2020) Tidal estuarine deposits of the transgressive Naturita Formation (Dakota Sandstone): San Rafael Swell, Utah, U.S.A. *J. Sediment. Res.*, **90**, 777–795.

Posamentier, H.W. and **Vail, P.R.** (1988) Eustatic controls on clastic deposition. II. Sequence and systems tract models. In: *Sea Level Changes – An Integrated Approach* (Eds Wilgus, C.K., Hastings, B.S., Kendall, C.G., St, C., Posamentier, H.W., Ross, C.A. and Van Wagoner, J.C.). *SEPM Spec. Publ.*, **42**, 125–154.

Poulsen, C.J., **Barron, E.J.**, **Peterson, W.H.** and **Wilson, P.A.** (1999) A reinterpretation of Mid-Cretaceous shallow marine temperatures through model-data comparison. *Paleoceanography*, **14**, 679–697.

Primm, J., **Johnson, C.** and **Stearns, M.** (2018) Basin-axial progradation of a sediment supply-driven distributive fluvial system in the Late Cretaceous southern Utah foreland. *Basin Res.*, **30**, 249–278.

Reeves Jr., C.C. (1970) Origin, classification and geologic history of caliche on the southern High Plains, Texas and eastern New Mexico. *J. Geol.*, **78**, 352–362.

Rittersbacher, A., **Howell, J.A.** and **Buckley, S.J.** (2014) Analysis of fluvial architecture in the Blackhawk

Formation, Wasatch Plateau, Utah, U.S.A., using large 3D photorealistic models. *J. Sediment. Res.*, **84**, 72–87.

Royse, F. (1993) Case of the phantom foredeep: early Cretaceous in west-central Utah. *Geology*, **21**, 133–136.

Rubin, D.M. and **McCulloch, D.S.** (1980) Single and superimposed bedforms: a synthesis of San Francisco Bay and flume observations. *Sediment. Geol.*, **26**, 207–231.

Ryer, T.A. (1983) Transgressive - regressive cycles and the occurrence of coal in some Upper Cretaceous strata of Utah. *Geology*, **11**, 207–210.

Schlesinger, W.H. (1985) The formation of caliche in soils of the Mojave Desert, California. *Geochim. Cosmochim. Acta*, **49**, 57–66.

Shanley, K.W. and **McCabe, P.J.** (1991) Predicting facies architecture through sequence stratigraphy - an example from the Kaiparowits Plateau, Utah. *Geology*, **19**, 742–745.

Shukla, U.K., **Singh, I.B.**, **Sharma, M.** and **Sharma, S.** (2001) A model of alluvial megafan sedimentation: Ganga Megafan. *Sediment. Geol.*, **144**, 243–262.

Sorensen, A.E. (2011) Geologic mapping of exhumed, mid-Cretaceous paleochannel complexes near Castle Dale, Emery County, Utah: On the correlative relationship between the Dakota Sandstone and the Mussentuchit Member of the Cedar Mountain Formation. MS Thesis, Brigham Young University, Provo, Utah, 67 pp.

Speed, C.M., **Sylvester, Z.**, **Flaig, P.P.**, **Durkin, P.**, **Cardenas, B.T.**, **Goudge, T.A.** and **Mohrig, D.** (2019) *Anatomy of a Fluvial Incision: Linking Geomorphology and Stratigraphy Using 3-D Outcrops of Exhumed Channel-Belt Deposits, Utah*. AAPG Annual Convention and Exhibition, San Antonio, Texas.

Sprinkel, D.A., **Madsen, S.K.**, **Kirkland, J.I.**, **Waanders, G.L.** and **Hunt, G.J.** (2012) Cedar Mountain and Dakota formations around Dinosaur National Monument: evidence of the first incursion of the Cretaceous Western Interior Seaway into Utah. *Utah Geol. Surv. Special Stud.*, **143**, 21.

Sprinkel, D.A., **Weiss, M.P.**, **Fleming, R.W.** and **Waanders, G.L.** (1999) Redefining the Lower Cretaceous stratigraphy within the central Utah foreland basin. *Utah Geol. Surv. Special Stud.*, **97**, 21.

Stokes, W.L. (1944) Morrison formation and related deposits in and adjacent to the Colorado Plateau. *Geol. Soc. Am. Bull.*, **55**, 951–992.

Suarez, C.A., **Gonzalez, L.A.**, **Ludvigson, G.A.**, **Kirkland, J.I.**, **Cifelli, R.L.** and **Kohn, M.J.** (2014) Multi-taxa isotopic investigation of paleohydrology in the Lower Cretaceous Cedar Mountain Formation, eastern Utah, U.S.A.: deciphering effects of the Nevadaplano Plateau on regional climate. *J. Sediment. Res.*, **84**, 975–987.

Tucker, R.T., **Zanno, L.E.**, **Huang, H.Q.** and **Makovicky, P.J.** (2020) A refined temporal framework for newly discovered fossil assemblages of the upper Cedar Mountain Formation (Mussentuchit Member), Mussentuchit Wash, Central Utah. *Cretac. Res.*, **110**, 104384.

Vaughn, R.L. and **Picard, M.D.** (1976) Stratigraphy, sedimentology, and petroleum potential of Dakota Formation, northeastern Utah: Uinta Basin. Rocky Mount. Assoc. Geol. Guidebook, 267–279.

Weissmann, G.S., **Hartley, A.J.**, **Nichols, G.J.**, **Scuderi, L.A.**, **Olson, M.**, **Buehler, H.** and **Banteah, R.** (2010) Fluvial form in modern continental sedimentary basins: distributive fluvial systems. *Geology*, **38**, 39–42.

Weissmann, G.S., **Hartley, A.J.**, **Scuderi, L.A.**, **Nichols, G.J.**, **Davidson, S.K.**, **Owen, A.**, **Atchley, S.C.**, **Bhattacharyya, P.**, **Chakraborty, T.**, **Ghosh, P.**, **Nordt, L.C.**, **Michel, L.** and **Tabor, N.J.** (2013) Prograding distributive fluvial systems-geomorphic models and ancient examples. *SEPM Spec. Publ.*, **104**, 131–147.

Weissmann, G.S., **Hartley, A.J.**, **Scuderi, L.A.**, **Nichols, G.J.**, **Owen, A.**, **Wright, S.**, **Felicia, A.L.**, **Holland, F.** and **Anaya, F.M.L.** (2015) Fluvial geomorphic elements in modern sedimentary basins and their potential preservation in the rock record: a review. *Geomorphology*, **250**, 187–219.

Williams, F.E. (1961) San Arroyo Gas Field, Grand County. *Utah Geol. Assoc., Oil and Gas Fields of Utah, A Symposium*, 4 p.

Williams, R.M.E., **Irwin, R.P.** and **Zimbelman, J.R.** (2009) Evaluation of paleohydrologic models for terrestrial inverted channels: implications for application to Martian sinuous ridges. *Geomorphology*, **107**, 300–315.

Williams, R.M.E., **Irwin, R.P.**, **Zimbelman, J.R.**, **Chidsey, T.C.** and **Eby, D.E.** (2011) Field guide to exhumed paleochannels near Green River, Utah: terrestrial analogs for sinuous ridges on Mars. *Spec. Pap. Geol. Soc. Am.*, **483**, 483–505.

Williams, R.M.E., **Chidsey, T.C.** and **Eby, D.E.** (2007) Exhumed paleochannels in Central Utah—Analogs for raised curvilinear features on Mars. In: *Central Utah—Diverse Geology of a Dynamic Landscape* (Eds G.C. Willis, M.D. Hylland, D.L. Clark and T.C. Chidsey), *Utah Geol. Assoc. Publ.*, **36**, 221–235.

Yamazaki, D., **Ikeshima, D.**, **Sosa, J.**, **Bates, P.D.**, **Allen, G.H.** and **Pavelsky, T.M.** (2019) MERIT Hydro: a high-resolution global hydrography map based on latest topography dataset. *Water Resour. Res.*, **55**, 5053–5073.

Young, R.G. (1960) Dakota group of Colorado Plateau. *Am. Assoc. Pet. Geol. Bull.*, **44**, 156–194.

Young, R.G. (1973) Depositional environments of basal Cretaceous rocks of the Colorado Plateau. In: *Cretaceous and Tertiary Rocks of the Southern Colorado Plateau* (Ed Fassett, J.E.). *Four Corners Geol. Soc. Memoir*, 10–27.

Manuscript received 27 April 2020; revision accepted 14 January 2021

APPENDIX

Outcrop localities

Location	Abbreviation	Latitude	Longitude	Data types
Last Chance Monocline	LCM	38°39′12.91″N	111°17′17.70″W	Reconnaissance
Mussentuchit Wash	MW	38°41′21.37″N	111°15′25.55″W	VOM, MS, palaeocurrent
Mesa Butte	MB	38°47′26.19″N	111°12′19.43″W	VOM, MS
I-70	I-70	38°49′24.82″N	111°11′6.48″W	VOM, MS
Moore Cutoff Road	MCR	38°56′47.57″N	111°4′22.17″W	VOM, MS, palaeocurrent
Ferron Creek	FC	39°6′58.02″N	110°57′40.90″W	Palaeocurrent
Channel at HH	CH	39°11′54.59″N	110°53′47.55″W	Palaeocurrent
Hadden Holes	HH	39°12′36.18″N	110°52′2.01″W	VOM, MS, palaeocurrent
Dinosaur Quarry Road	DQR	39°19′58.08″N	110°45′6.98″W	Reconnaissance
Price River	PR	39°25′30.14″N	110°37′14.90″W	VOM, MS, palaeocurrent
Grassy Trail Creek	GTC	39°24′42.35″N	110°29′30.19″W	Reconnaissance
Green River Cutoff Road	GRCR	39°11′58.58″N	110°22′30.24″W	VOM, MS, palaeocurrent
Lost Spring Wash	LSW	39°5′42.12″N	110°21′23.68″W	Reconnaissance
Buckmaster Draw	BD	38°57′48.29″N	110°22′4.36″W	Reconnaissance
Green River Airport	GRA	38°56′59.60″N	110° 9′59.60″W	VOM, MS, palaeocurrent
Southwest Green River	SWGR	38°52′34.36″N	110°16′16.32″W	VOM, MS, palaeocurrent
New Area 51	N51	38°58′2.04″N	110°7′20.67″W	Palaeocurrent
Ruby Ranch Road	RRR	38°51′15.30″N	109°58′58.00″W	VOM, MS, palaeocurrent
Klondike Bluffs	KB	38°46′13.95″N	109°42′56.64″W	Reconnaissance
Long Valley	LV	38°52′13.30″N	109°42′48.70″W	VOM, MS, palaeocurrent
Utahraptor Ridge	URR	38°50′53.55″N	109°39′23.35″W	VOM, MS, palaeocurrent
Yellow Cat Road	YCR	38°51′27.38″N	109°32′42.01″W	Reconnaissance
Poison Strip	PS	38°52′36.58″N	109°26′17.32″W	Reconnaissance
Owl Draw Road	ODR	38°51′34.13″N	109°20′37.84″W	VOM, MS, palaeocurrent
Caineville Reef North	CRN	38°28′54.76″N	110°56′36.54″W	VOM, MS, palaeocurrent
Fig. 4A		38°50′26.54″N	109°56′44.47″W	Palaeocurrent, MS
Fig. 4B		38°52′34.36″N	110°16′16.32″W	Palaeocurrent, MS
Fig. 4C		38°51′37.37″N	109°39′14.93″W	Palaeocurrent, MS